



# Constitutive Modeling of Structural Steels: Nonlinear Isotropic/Kinematic Hardening Material Model and Its Calibration

Alexander R. Hartloper, S.M.ASCE<sup>1</sup>; Albano de Castro e Sousa<sup>2</sup>; and Dimitrios G. Lignos, M.ASCE<sup>3</sup>

Abstract: Numerical models of structural components that deteriorate primarily due to geometric instabilities under multiaxis cyclic loading are sensitive to both the assumed geometric imperfections and the nonlinear material model assumptions. Therefore, the accuracy of the constitutive model is a desirable feature in finite-element simulations. However, the classic Voce-Chaboche metal plasticity model, ubiquitous among commercial finite-element software, is found to underestimate the initial yield stress in structural steels by about 10%–30% when calibrated to minimize the overall difference in strain energy between the model and test data of load protocols representative of earthquake loading. This paper proposes a refined version of the Voce-Chaboche material model. When compared with the original model, the updated one improves the prediction of the initial yield stress, can simulate initial yield plateau behavior, and better estimates experimental cyclic stress-strain data. Constraints on the model parameters are established, a calibration procedure is developed, and model parameters are proposed for nine structural steels used worldwide. Source code for the material model is also made publicly available. A case study demonstrates that steel component behavior is sensitive to subtle differences in the material response that arise between the Voce-Chaboche and the proposed material models. **DOI:** 10.1061/(ASCE)ST.1943-541X.0002964. © 2021 American Society of Civil Engineers.

**Author keywords:** Constitutive model; Structural steel; Discontinuous yielding; Multiaxial plasticity; Earthquake loading; Nonlinear inverse problem; Geometric instabilities.

#### Introduction

Experimental evaluation and accurate numerical modeling of structural components and systems are necessary for the field of earth-quake engineering to evaluate component behavior under multiaxis cyclic loading. In steel structures, which form the basis of this paper, parametric full-scale physical experiments would often require an inordinate amount of resources. Furthermore, the complex interactions between nonlinear material behavior and the geometric nonlinearities are challenging to study analytically. In contrast, numerical modeling in the form of continuum finite-element (CFE) analysis is a well-established alternative to investigate these problems in a so-called virtual testing environment (ATC 2017). A few prevalent examples demonstrating the use of CFE analysis include modeling braces and brace connections in concentrically braced

<sup>1</sup>Doctoral Assistant, École Polytechnique Fédérale de Lausanne, School of Architecture, Civil and Environmental Engineering IIC, Resilient Steel Structures Laboratory (EPFL ENAC IIC RESSLab), GC B3 514, Station 18, Lausanne 1015, Switzerland. ORCID: https://orcid.org/0000-0003-3120-1748. Email: alexander.hartloper@epfl.ch

<sup>2</sup>Postdoctoral Research Scientist, École Polytechnique Fédérale de Lausanne, School of Architecture, Civil and Environmental Engineering IIC, Resilient Steel Structures Laboratory (EPFL ENAC IIC RESSLab), GC B3 465, Station 18, Lausanne 1015, Switzerland. Email: albano.sousa@epfl.ch

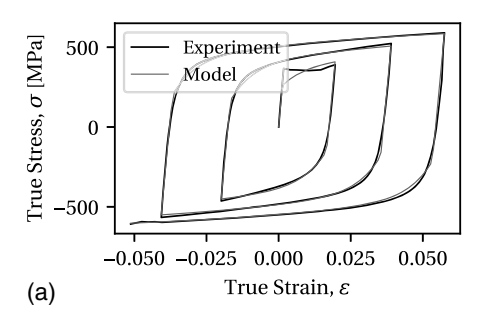
<sup>3</sup>Associate Professor, École Polytechnique Fédérale de Lausanne, School of Architecture, Civil and Environmental Engineering IIC, Resilient Steel Structures Laboratory (EPFL ENAC IIC RESSLab), GC B3 485, Station 18, Lausanne 1015, Switzerland (corresponding author). Email: dimitrios.lignos@epfl.ch

Note. This manuscript was submitted on December 6, 2019; approved on November 23, 2020; published online on January 30, 2021. Discussion period open until June 30, 2021; separate discussions must be submitted for individual papers. This paper is part of the *Journal of Structural Engineering*, © ASCE, ISSN 0733-9445.

frames (Fell et al. 2009; Hsiao et al. 2012), studying geometric instability mechanisms in commonly used lateral load resisting systems (Imanpour et al. 2016), extending results from full-scale steel wide-flange column tests to a wide range of column geometries and loading conditions (Fogarty and El-Tawil 2016; Elkady and Lignos 2015, 2018b), and aiding the development of component modeling guidelines in support of performance-based earthquake engineering (Lignos et al. 2019).

Accurately simulating geometric instabilities and nonlinear material behavior is essential in understanding the performance of components subjected to seismic demands through CFE analysis. At the crux of this issue is the choice of initial geometric imperfections to induce an appropriate geometrically nonlinear response, as well as the choice of a material model that rigorously represents the material behavior. Geometric imperfections are typically included by superimposing scaled elastic buckling modes found through eigenvalue analysis, and the sensitivity of simulations to both the shape and amplitude of the imperfections has been acknowledged (Schafer et al. 2010; Kalochairetis and Gantes 2011; Elkady and Lignos 2015, 2018b; Ziemian et al. 2018; Cravero et al. 2020). However, none of these studies have investigated the sensitivity of steel component simulations to the choice of material model and its parameters—this paper works toward addressing these questions.

The employed material model should capture pertinent cyclic loading effects, notably the Bauschinger effect, cyclic hardening, and ratcheting (Sowerby et al. 1979; Cofie and Krawinkler 1985; Hassan and Kyriakides 1992; Kaufmann et al. 2001). Cyclic softening is another effect observed in particular steels (Hassan and Kyriakides 1992); however, this effect is not present in the mild structural steels that are the focus of this research. Mild steels are subsequently defined as steels that contain less than 0.3% carbon by mass. The constitutive model combining the nonlinear isotropic hardening law proposed by Voce (1948) to model cyclic hardening with the nonlinear kinematic hardening law by Chaboche et al. (1979) to



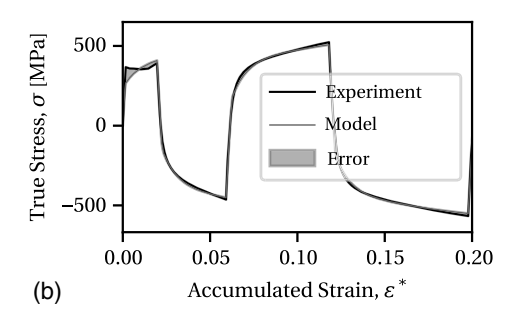


**Fig. 1.** Uniaxial 2% increasing strain amplitude cyclic coupon test on S355J2+N steel and its best-fit Voce-Chaboche model prediction: (a) comparison of test and model responses; and (b) model error in initial cycles. (Experimental data from Grigoriou and Lignos 2017.)

model the Bauschinger effect and ratcheting, in this study referred to as the Voce-Chaboche model, is ubiquitous among commercial finite-element software.

In the context of earthquake loading, constitutive models for mild structural steels should be able to closely replicate the material's behavior regardless of the load history to account for the effect of ground motion uncertainty on the structural response. de Castro e Sousa et al. (2020) addressed this issue by calibrating the Voce-Chaboche model using data sets of 5–10 uniaxial round-bar coupon tests subjected to distinct cyclic strain histories deemed to be representative of earthquake loading by Suzuki (2018). The reader is directed to the study by de Castro e Sousa et al. (2020) for a detailed discussion of alternative calibration methods. The calibration method of de Castro e Sousa et al. (2020) also reveals that there is an inherent issue in the Voce-Chaboche model for the modelization of mild structural steels in this context.

The issue in the Voce-Chaboche model for mild steels is related to the discontinuous yielding phenomenon (Hall 1970; Lubliner 2008) and manifests itself in an underestimation of the initial yield stress with the aforementioned methodology. de Castro e Sousa et al. (2020) demonstrate that the overall difference in the accumulated strain energy between the model and the test data is minimized by sacrificing accuracy in the initial yield stress to better predict the behavior in further plastic loading cycles. Their study suggests that the model's optimal initial yield stress underestimates the experimentally measured yield stress by around 10%-30% depending on the data set considered, and the reason for this will be discussed subsequently. Note that there is no discernible bias in the underestimation based on the steels' yield stress, manufacture provenance, or chemical composition for the sets of structural steels investigated by de Castro e Sousa et al. (2020). The underestimation of the initial yield stress should be addressed in an effort to investigate the sensitivity of steel components to the choice of the material model and its input parameters.

The objective of this paper is to propose an updated Voce-Chaboche (UVC) material model that better estimates the initial yield stress for structural steels without reducing the fidelity in later loading cycles. An improvement in the prediction of the yield stress at the material level has implications for the extent of member yielding and, subsequently, the simulated geometric instabilities in components—both these aspects are demonstrated subsequently in this paper through a case study. In turn, accurate predictions of member buckling are important when simulating structures at limit states in which such component deterioration is expected. A refined isotropic hardening rule is proposed to achieve this goal, and constraints on the material model parameters that form the sufficient condition to ensure instantaneous hardening of the material model are established. These constraints are considered to be essential for the proper use of the proposed material model for structural steels.

A calibration procedure is also proposed that, in combination with the parameter constraints, is general and agnostic with respect to the material model, i.e., no further engineering heuristics are introduced. Finally, we demonstrate that steel components subjected to mulitaxis cyclic loading may be highly sensitive to the material model assumptions. A case study utilizing a steel wide-flange column model under compressive axial load coupled with cyclic lateral drift demands demonstrates that seemingly small changes in the material model parameters can have a significant influence on the simulation results.

# Limitation of the Voce-Chaboche Model for Mild Steels

The Voce-Chaboche material model underestimates the yield stress in mild structural steels as a compromise to reduce the overall difference in accumulated strain energy between stress-strain data and the model prediction for cyclic loading histories. This issue is illustrated using data from a cyclic uniaxial 2% increasing strain amplitude test on S355J2+N steel (CEN 2005b) with a nominal yield stress of  $f_v = 355$  MPa [the experimental data is from Grigoriou and Lignos (2017)]. Test data true stress-strain relations are shown along with the best-fit Voce-Chaboche model prediction in Fig. 1(a). Best-fit in the context of this paper is defined as the set of parameters that minimizes the accumulated squared area, i.e., squared strain energy, between the experiment and the model prediction. This error is represented by the shaded region in Fig. 1(b) restricted on the first few cycles of loading in Fig. 1(a). Notice that the initial yield stress of the test data is underestimated by the model to match better the stress-strain history in subsequent cycles, which tend to present a lower elastic limit with smooth plastic hardening. Consequently, the error is primarily focused on the first loading cycle due to the mismatch of the yield stress. The observation that the initial yield stress is greater than in ensuing cycles, seen in the light of  $J_2$  plasticity, implies that the size of the yield surface diminishes after initial plastic straining.

The reduction in the elastic limit after the initiation of plastic straining is attributed to interstitial carbon and nitrogen atoms in the crystal lattice (Cottrell and Bilby 1949; Hall 1970; Lubliner 2008). These atoms concentrate in the tension field surrounding dislocations, forming a so-called atmosphere, initially locking the dislocations into place (Haidemenopoulos 2018). The yield plateau is the strain range characterized by the growth of Luders bands due to the successive stripping of dislocations from their atmospheres as deformation progresses. A typical stress-strain response for mild structural steels, including the plateau region, is shown schematically in Fig. 2. The Luders strain,  $\varepsilon_L$ , denoting the end of the yield plateau, is observed to be around 2% strain in mild

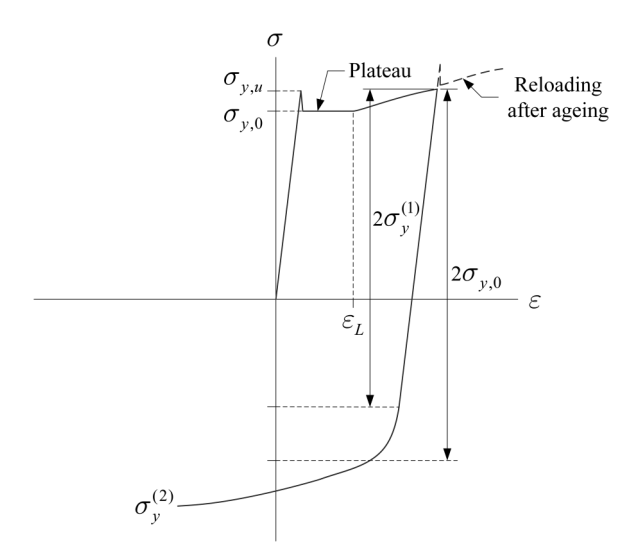


**Fig. 2.** Schematic illustration of initial structural steel material response to cyclic loading.

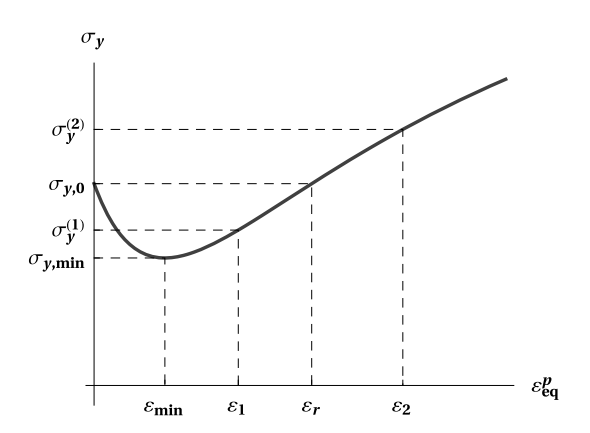


**Fig. 3.** Schematic illustration of the yield surface progression for structural steels.

steels (Lemaitre and Chaboche 1990). No plateau is observed upon further loading or immediate reloading once the accumulated plastic strain is greater than the Luders strain. However, a secondary upper yield point is observed if sufficient time is provided for the reformation of atmospheres; this is known as the strain-aging effect (Hall 1970; Lubliner 2008).

The solid load path in Fig. 2 represents immediate loading up to the second excursion of the test depicted in Fig. 1(a). The dashed loading path in this figure represents the expected behavior if the test was unloaded for a period (on the order of days) then reloaded in tension. Note that the secondary upper yield point formed after aging exceeds the stress upon immediate reloading. Consideration of the strain aging effect is potentially critical in studying main-shock/after-shock problems in which the steel material has time to age after the initial plastic straining; however, this subject is outside the scope of the present paper.

In Fig. 1(a), the difference between the initial plateau yield stress,  $\sigma_{y,0}$ , and the reduced yield stress upon immediate reloading in compression,  $\sigma_y^{(1)}$ , is highlighted. Progression of the size of the yield surface,  $\sigma_y$ , for mild steels undergoing the same loading path is shown schematically in Fig. 3 with respect to the equivalent plastic strain,  $\varepsilon_{eq}^p$ . The initial decrease in size from  $\varepsilon_{eq}^p = [0, \varepsilon_{\min}]$  is

intended to simulate the stripping of dislocations from their atmospheres, the later increase after this range accounts for cyclic hardening due to increasing dislocation densities (Lemaitre and Chaboche 1990).

We propose a refined material model that accounts for the reduction in the size of the yield surface in mild structural steels by modifying the Voce isotropic hardening rule. The isotropic hardening rule used by Voce (1948) is defined in Eq. (1)

$$\sigma_{y} = \sigma_{y,0} + Q_{\infty}(1 - \exp[-b\varepsilon_{eq}^{p}]) \tag{1}$$

where  $\sigma_{y,0}$  = initial yield stress; and  $Q_{\infty}$  and b are material parameters that define the magnitude and rate of isotropic hardening, respectively. The Voce isotropic hardening rule is monotonically increasing and cannot represent the sort of behavior shown in Fig. 3. Therefore, parameters will be added to this isotropic hardening rule that impose an initial decrease in the size of the yield surface. The following section discusses the formulation of the proposed material model, followed by its numerical implementation and calibration.

# **Proposed Material Model**

The proposed material model follows a classic small-strain, rate-independent plasticity formulation (Simo and Hughes 1998). Geometrically nonlinear problems should be addressed at the material level through an objective integration algorithm, as described by Simo and Hughes (1998); however, this discussion is excluded in this study for brevity. Some notation used in this paper is established for clarity before proceeding with the description of the model.

Scalar quantities are not bolded (e.g., a). Bold, serif symbols are first-order tensors (vectors) or second-order tensors (e.g., b), and capitalized, bold symbols are fourth-order tensors (e.g., C). The second-order identity tensor is  $\mathbf{I}$ , the fourth-order symmetric identity tensor is  $\mathbf{I}$ , and the fourth-order deviatoric unit tensor is  $\mathbf{I}_{\text{dev}}$ —definitions for each are provided in the Notation. Contraction on two indices is  $\mathbf{b}:\mathbf{b} = \sum_i \sum_j b_{ij} b_{ij}$ ; the tensor product is  $\mathbf{b} \otimes \mathbf{b} = b_{ij} b_{kl}$ ; the deviatoric part of a tensor is  $\text{dev}[\mathbf{b}] = \mathbf{I}_{\text{dev}} \cdot \mathbf{b}$ ; and the 2-norm is always used, i.e.,  $||\mathbf{b}|| = \sqrt{\mathbf{b}:\mathbf{b}}$ .

#### Constitutive Equations

This paper proposes an updated Voce-Chaboche model, denoted as the UVC model. The UVC model uses an additive decomposition of the strain tensor,  $\varepsilon$ , defined in Eq. (2)

$$\boldsymbol{\varepsilon} = \boldsymbol{\varepsilon}^e + \boldsymbol{\varepsilon}^p \tag{2}$$

where  $e^e$  = elastic strain tensor; and  $e^p$  = plastic strain tensor. The elastic stress-strain relation is provided in Eq. (3)

$$\sigma = \mathbf{C}: (\boldsymbol{\varepsilon} - \boldsymbol{\varepsilon}^p) \tag{3}$$

where  $\sigma$  = stress tensor; and C = isotropic tensor of elastic moduli. A precise definition of C is provided in the Notation. The von Mises yield condition is used in Eq. (4) for the yield function f

$$f = \sqrt{(\operatorname{dev}[\boldsymbol{\sigma}] - \operatorname{dev}[\boldsymbol{\alpha}]) : (\operatorname{dev}[\boldsymbol{\sigma}] - \operatorname{dev}[\boldsymbol{\alpha}])} - \sqrt{2/3}\sigma_{y}$$
$$= \|\boldsymbol{\xi}\| - \sqrt{2/3}\sigma_{y} \le 0 \tag{4}$$

where  $\alpha$  = overall backstress;  $\xi = \text{dev}[\sigma] - \text{dev}[\alpha]$  is the deviatoric relative stress; and  $\sigma_y$  = yield stress of the material. In accordance with the principle of maximum plastic dissipation (Simo and Hughes 1998), the flow rule in Eq. (5) associated with  $J_2$  plasticity is

$$\dot{\boldsymbol{\varepsilon}}^p = \lambda \frac{\boldsymbol{\xi}}{\|\boldsymbol{\xi}\|} = \lambda \boldsymbol{n} \tag{5}$$

where the overdot indicates the time derivative;  $\lambda = \text{consistency}$  parameter (which is equivalent to the time derivative of the plastic multiplier); and  $\mathbf{n} = \mathbf{\xi}/\|\mathbf{\xi}\|$  is the unit normal to the yield surface in the deviatoric stress space. For the associative flow rule, the equivalent plastic strain is defined by Eq. (6)

$$\dot{\varepsilon}_{eq}^p = \sqrt{2/3}\lambda\tag{6}$$

Armstrong and Frederick (1966) defined the nonlinear kinematic hardening rule in Eq. (7) for a single backstress component k

$$\dot{\boldsymbol{\alpha}}_{k} = \sqrt{2/3} C_{k} \dot{\boldsymbol{\varepsilon}}_{eq}^{p} \boldsymbol{n} - \gamma_{k} \dot{\boldsymbol{\varepsilon}}_{eq}^{p} \boldsymbol{\alpha}_{k} \tag{7}$$

where  $C_k$  and  $\gamma_k$  = parameters associated with the magnitude and rate of backstress component k, respectively. Chaboche et al. (1979) later proposed to use a summation of  $N_k$  backstress terms as an improvement to the Armstrong-Frederick rule so that the overall backstress defined in Eq. (8) is

$$\alpha = \sum_{k=1}^{N_k} \alpha_k \tag{8}$$

We propose an update to the isotropic hardening rule to account for the decrease in the initial yield stress for mild structural steels

$$\sigma_{y} = \sigma_{y,0} + Q_{\infty}(1 - \exp[-b\varepsilon_{eq}^{p}]) - D_{\infty}(1 - \exp[-a\varepsilon_{eq}^{p}]) \quad (9)$$

where  $D_{\infty}$  and a = material parameters that define the magnitude and rate of the decrease in the initial yield stress. As previously discussed, Eq. (9) is valid for immediate unloading/reloading of the material. The novelty in the proposed model is that the additional term is able to account for the discontinuous yielding phenomenon without leading to a loss of accuracy in later loading cycles by initially reducing the yield surface. This behavior is accomplished through the modification to the isotropic hardening rule and by imposing the proposed constraints on the parameters to enforce nonsoftening behavior. Such a consideration is paramount when calibrating the model using multiple load protocols in an effort to reduce uncertainty in the predicted material behavior when subjected to random strain histories. Additionally, the term is incorporated in a smooth functional form without any discrete imposition of loading stages. Note that the original Voce-Chaboche model can be recovered by simply setting  $D_{\infty} = 0$  and  $a \neq 0$ , where  $a \neq 0$  is required for numerical reasons in the algorithmic implementation.

Numerous other models exist in the literature for modeling mild structural steels; a nonexhaustive list includes studies by Ohno (1982), Cofie and Krawinkler (1985), Yoshida and Uemori (2002), Ucak and Tsopelas (2011), Mahan et al. (2011), Budaházy and Dunai (2013), and Hu et al. (2018). Most of the reviewed models have a multisurface formulation and are not discussed further as the simplicity of the algorithmic implementation for isotropic/ kinematic hardening is preferred. The model by Budaházy and Dunai (2013) has a multilinear isotropic hardening component to simulate the upper yield stress and plateau and dynamically updates the material parameters depending on the applied load for uniaxial stress states; however, a single set of parameters for all loading scenarios is preferred for its simplicity. The two nonlinear isotropic/kinematic hardening models by Ucak and Tsopelas (2011) and Hu et al. (2018) share common features with the UVC model. Notably, both models include a term similar to the  $D_{\infty}$  term of the proposed model. The highlighted differences with the UVC

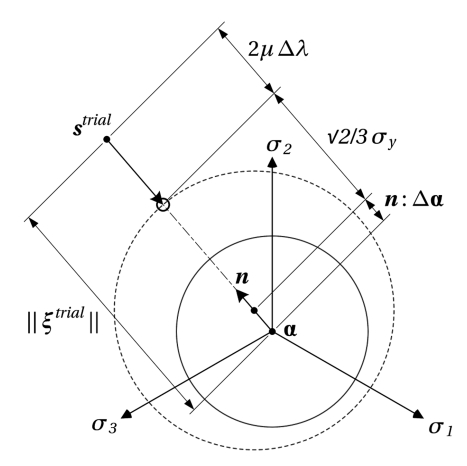


Fig. 4. Schematic illustration of the radial return mapping algorithm.

model are that these two models consider distinct plateau and hardening phases, the term similar to  $D_{\infty}$  only provides cyclic softening in the plateau region, and the constraints on the set of parameters are not as general as those discussed subsequently in this paper because parameter bounds are tied to particular steel material.

# Numerical Implementation

The numerical implementation of the proposed material model follows two parts: first, the solution of the consistency condition to determine the stress for a given strain increment and, second, the production of the consistent tangent moduli for use in an iterative nonlinear finite-element analysis procedure.

# Solution to the Consistency Condition

The return mapping (implicit backward-Euler) time integration algorithm is implemented to provide the stress for given strain states (Simo and Hughes 1998). Notions of plastic loading and elastic unloading are represented by the Karush-Kuhn-Tucker complementary conditions in Eq. (10)

$$\lambda \ge 0, \quad f \le 0, \quad \lambda f = 0 \tag{10}$$

These conditions establish the elastic-predictor-plastic-corrector methodology, whereby if the assumed elastic trial state violates the yield condition, then plastic loading is active. The algorithm is implemented as a strain driven problem (Simo and Hughes 1998), i.e., let  $t \in [0, t_1, \ldots, T] \subset \mathbb{R}$  be the discretized time interval of interest. At time  $t_n$ , we assume that the total strain, plastic strain, and internal variables are known. If plastic loading is activated, the objective is to solve for the increment in the plastic multiplier,  $\Delta \lambda = \int_{t_n}^{t_{n+1}} \lambda dt$ , that constrains the stress state to the yield surface.

Fig. 4 illustrates the algorithmic counterpart to the consistency condition that arises for multiaxial stress states with a von Mises yield potential in the  $\pi$ -plane (i.e., radial return mapping). Satisfying this condition for  $\Delta\lambda$  is equivalent to finding the orthogonal projection of the trial stress state onto the hardened yield surface (Simo and Hughes 1998). In this figure,  $s^{\text{trial}}$  is the deviatoric trial stress at the start of a particular increment,  $n:\Delta\alpha$  is the increment in kinematic hardening,  $\sqrt{2/3}\sigma_y$  is the equivalent yield stress, and  $2\mu\Delta\lambda$  is the reduction in the magnitude of the trial stress to account for the increment in the plastic strain in accordance with Eq. (3). The radial return mapping algorithm balances all these components by solving for  $\Delta\lambda$  at each time increment.

Starting at time  $t_n$ , Eq. (11) represents the algorithmic consistency condition to be solved at time increment  $t_{n+1}$ 

$$g(\Delta\lambda) = \|\boldsymbol{\xi}_{n+1}^{\text{trial}}\| - \left(\sqrt{\frac{2}{3}}\sigma_{y,n+1} + 2\mu\Delta\lambda + \boldsymbol{n}_{n+1}:\Delta\boldsymbol{\alpha}\right) = 0 \tag{11}$$

where  $\Delta \alpha = \alpha_{n+1} - \alpha_n$ . The consistency condition for the time step  $t_{n+1}$  is solved through iterations over i using Newton's local method (Bierlaire 2015)

$$\Delta \lambda^{(i+1)} = \Delta \lambda^{(i)} - \frac{g(\Delta \lambda^{(i)})}{Dg(\Delta \lambda^{(i)})}$$
 (12)

where the linearization of Eq. (11) is provided in Eq. (13)

$$Dg(\Delta\lambda) = \frac{\partial g(\Delta\lambda)}{\partial \Delta\lambda} = -2\mu \left(1 + \frac{H'_{n+1} + K'_{n+1}}{3\mu}\right) \tag{13}$$

The kinematic and isotropic hardening moduli for multiaxial loading are respectively defined by Eqs. (14) and (15)

$$H'_{n+1} = \sum_{k} (C_k e_{k,n+1}) - \sqrt{\frac{3}{2}} n_{n+1} : \sum_{k} (\gamma_k e_{k,n+1} \alpha_{k,n})$$
 (14)

$$K'_{n+1} = Q_{\infty}b \exp[-b\varepsilon^{p}_{ea,n+1}] - D_{\infty}a \exp[-a\varepsilon^{p}_{ea,n+1}]$$
 (15)

where

$$e_{k,n+1} = \exp[-\gamma_k(\varepsilon_{eq,n+1}^p - \varepsilon_{eq,n}^p)]$$
 (16)

For multiaxial loading, Eq. (12) is iterated until a tolerance of  $|g(\Delta\lambda)| < 10^{-10}$  is satisfied. Full details of the radial return mapping procedure, along with efficient algorithms for uniaxial, multiaxial, and plane-stress, are provided in the study by Hartloper et al. (2019).

# Consistent Tangent Moduli

The elastoplastic tangent moduli consistent with the return mapping algorithm (Simo and Hughes 1998) are now provided for the case of plastic loading. For brevity, only the final result is shown, and details of the derivation can be found in the study by Hartloper et al. (2019). The consistent elastoplastic tangent moduli are defined by the fourth-order tensor  $\mathbf{C}_{n+1}^{ep}$  in Eq. (17)

$$\mathbf{C}_{n+1}^{ep} = \kappa(\mathbf{1} \otimes \mathbf{1}) + 2\mu\theta_1 \left( \mathbf{I} - \frac{1}{3}\mathbf{1} \otimes \mathbf{1} \right)$$
$$-2\mu\theta_2(\mathbf{n}_{n+1} \otimes \mathbf{n}_{n+1}) + 2\mu\theta_3(\mathbf{n}_{n+1} \otimes \Delta\boldsymbol{\alpha}) \quad (17)$$

where

$$\theta_{1} = 1 - \frac{2\mu\Delta\lambda}{\|\boldsymbol{\xi}_{n+1}^{\text{trial}}\|}, \qquad \theta_{2} = \left(\frac{1}{\beta} + \frac{\boldsymbol{n}_{n+1}:\Delta\boldsymbol{\alpha}}{\theta_{3}}\right) - (1 - \theta_{1}),$$

$$\theta_{3} = \frac{1}{\beta\|\boldsymbol{\xi}_{n+1}^{\text{trial}}\|}$$
(18)

and

$$\beta = 1 + \frac{K'_{n+1} + H'_{n+1}}{3\mu} \tag{19}$$

A symmetric approximation of the tangent moduli is used because the last term in Eq. (17) is asymmetric, and therefore

$$\mathbf{C}_{sym.,n+1}^{ep} = \frac{1}{2} ((\mathbf{C}_{n+1}^{ep})^T + \mathbf{C}_{n+1}^{ep})$$
 (20)

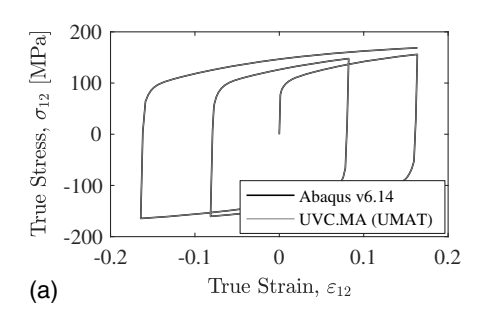
Hopperstad and Remseth (1995) show that using a symmetric approximation preserves the quadratic convergence of the global Newton solution procedure. This result suggests that the symmetric approximation leads to an overall reduction in both computer memory use and the number of computations required because symmetric matrix storage and solvers can be employed.

#### Validation

The proposed material model is implemented in the nonlinear finite-element software ABAQUS (2014) and the Open System for Earthquake Engineering Simulation (OpenSees version 3.2.0) (McKenna 1997) for multiaxial, plane-stress, and uniaxial stress states. User subroutine files (UMATs) for Abaqus and C++ source code with compiled dynamic link libraries (.dlls) for OpenSees are made publicly available (Hartloper 2019). The implementations are validated by comparing the response of several finite-element models using the UMAT and NDMaterial with equivalent models using the built-in nonlinear isotropic/kinematic model in Abaqus version 6.14 (ABAQUS 2014). In all these validation cases, the updated isotropic hardening rule of the proposed material model is neglected by simply setting  $D_{\infty} = 0$  and a = 1 (the choice of a=1 is made for simplicity as long as  $a \neq 0$ ). Material properties representative of an ASTM A992 (ASTM 2015) Gr. 50 steel (nominal  $f_v = 345$  MPa) are assumed for all analyses: E =179,800 MPa,  $\nu$  = 0.3,  $\sigma_{y,0}$  = 318.5 MPa,  $Q_{\infty}$  = 100.7 MPa, b = 8.0,  $D_{\infty}$  = 0.0 MPa, a = 1.0,  $C_{1}$  = 11,608.2 MPa,  $\gamma_{1}$  = 145.2,  $C_2 = 1,026.3 \text{ MPa}$ , and  $\gamma_2 = 4.7$ . Only two cases are provided in this paper for brevity, but several more validations are provided in the study by Hartloper et al. (2019).

A unit cube model subjected to biaxial loading demonstrates that the material model implementation is accurate when compared with the built-in Abaqus v6.14 material model. Unit cube models consisting of a single fully-integrated brick element (Abaqus: C3D8; OpenSees: SSPbrick) are subjected to two biaxial stress states in Abaqus and OpenSees. Results from both the implemented multiaxial UMAT [UVC.MA (UMAT)] and the implemented multiaxial NDMaterial [UVC.MA (NDM)] are compared with the results from the built-in nonlinear isotropic/kinematic model in Abaqus v6.14 (ABAQUS). Comparisons of the results are shown in Figs. 5(a and b). Both implementations agree with the built-in Abaqus results to the level of machine precision, highlighting the accuracy of the implemented radial return mapping procedure and the consistency of the tangent moduli with the material response.

The material model implementations are also accurate and efficient for component level simulations. The plane stress implementation is validated by modeling a cantilever column using shell elements (S4R) in Abaqus. The column cross-section is a W360X122 (W14X82 in US customary units), a constant compressive axial load equal to 20% of the axial yield strength is applied, and the symmetric cyclic load protocol from Chapter K of AISC (2016) is applied at the column top. The column model is developed according to the recommendations by Elkady and Lignos (2018b). For further details on the modeling procedure, loading, and boundary conditions, see the study by Hartloper et al. (2019). Fig. 6 shows that there is a negligible difference in the momentrotation between the models using the built-in material (ABAQUS) and the implemented material [UVC.PS (UMAT)]. These differences are attributed to accumulated errors that arise from a difference in the number of required iterations between the two models (UVC. PS UMAT: 4231; ABAQUS: 8583). The model run using the UVC. PS UMAT requires approximately 50% fewer iterations than the



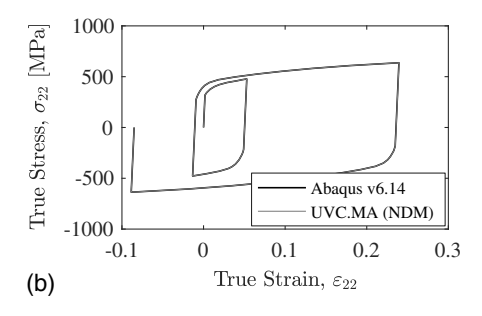


Fig. 5. Results from the material model unit cube validation studies: (a) Abaqus UMAT validation; and (b) OpenSees NDMaterial validation.

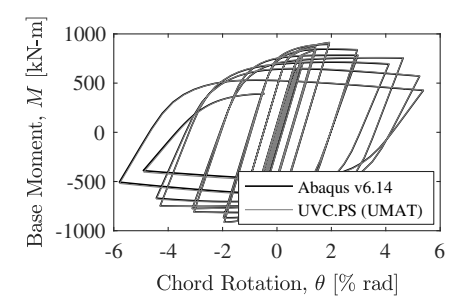


Fig. 6. Results from the material model column validation study.

one using the built-in material model, likely because large plastic strain increments can be converged by the implemented UMAT, whereas the built-in material model reduces the time step to achieve convergence. In relation to the preceding discussion, the implemented UMAT is more efficient than the built-in Abaqus v6.14 material model in this case.

# Constraints on the Parameter Space to Ensure Nonsoftening

Constraints on the parameter space are necessary because an incorrect choice of parameters for the proposed material model may violate the instantaneous strain-hardening behavior of mild steel materials. Establishing a nonnegative tangent modulus for all plastic strain values, e.g., perfectly-plastic or strain-hardening materials, is used as the starting point for the derivations in this section. This condition is first developed for uniaxial stress states. Afterward, this condition is shown to enforce the uniqueness of the elastoplastic boundary value problem for all stress states.

#### **Uniaxial Loading**

The algorithmic tangent modulus for a uniaxial stress state is given in Eq. (21) (Simo and Hughes 1998)

$$C_u^{ep} = \frac{E(K_u' + H_u')}{E + K_u' + H_u'} \tag{21}$$

where E = elastic modulus; and the kinematic and isotropic hardening moduli are respectively defined for uniaxial loading by Eqs. (22) and (23)

$$H'_{u} = \sum_{k} (C_{k} - \operatorname{sign}[\sigma - \alpha] \gamma_{k} \alpha_{k})$$
 (22)

$$K_{u}' = Q_{\infty}b \exp[-b\varepsilon_{eq}^{p}] - D_{\infty}a \exp[-a\varepsilon_{eq}^{p}]$$
 (23)

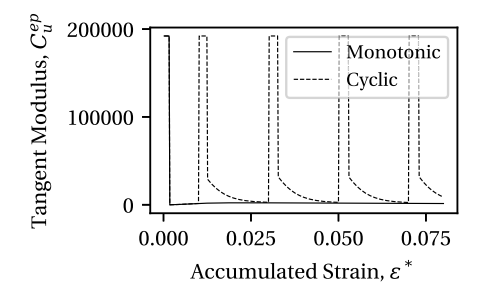


**Fig. 7.** Tangent modulus of the proposed material model subjected to monotonic and cyclic loading histories.

If  $K'_u + H'_u \ge 0$ , the tangent modulus in Eq. (21) is nonnegative because E is a positive parameter. Therefore, we just seek to impose the condition  $K'_u + H'_u \ge 0$  as the case  $-(K'_u + H'_u) \ge E$  is ignored because we desire a nonsoftening response.

The value of  $K'_u + H'_u$  may be less than zero if the  $D_{\infty}$  and aparameters in the isotropic hardening are not properly chosen. Ensuring  $C_u^{ep} \ge 0$  is further complicated by the path-dependency of the kinematic hardening term. A key result used to resolve the path-dependency is that the least tangent modulus is found if the strain is monotonically increasing in tension or compression. This fact is shown in Fig. 7 that illustrates the tangent modulus for monotonic tensile (solid line) and cyclic tension/compression loading histories (dashed line) using Eq. (21). The peaks and plateaus in the tangent modulus of the cyclic loading history shown in this figure correspond to elastic unloading/reloading. In turn, the plateaus are followed by a gradual decrease in the value of  $C_u^{ep}$  to the limit of monotonic loading with further plastic straining. From Eq. (7), the monotonic tensile loading provides the lower-bound tangent modulus at all points because reversal in the loading direction decreases the value of  $\alpha$ , thereby increasing the value of  $H'_{\mu}$  in Eq. (22). It follows that the material is nonsoftening under uniaxial loading for all strain histories if the minimum of the monotonic tangent modulus is restricted to be always nonnegative.

Monotonic tensile/compressive loading from an initial state of zero plastic strain is used as a starting point to develop the parameter constraints. Under these two assumptions, the uniaxial kinematic hardening modulus is defined by Eq. (24)

$$H'_{u,\text{mono}} = \sum_{k} (C_k \exp[-\gamma_k \varepsilon_{eq}^p])$$
 (24)

while the isotropic hardening modulus is unaffected by this assumption. Replacing Eq. (22) with Eq. (24) in Eq. (21), the constraint that defines nonsoftening behavior is provided in Eq. (25)

$$\hat{g} = D_{\infty} a \exp[-a\varepsilon_{eq}^{p}] - Q_{\infty} b \exp[-b\varepsilon_{eq}^{p}] - \sum_{k} (C_{k} \exp[-\gamma_{k}\varepsilon_{eq}^{p}]) \le 0$$
(25)

This constraint implies that the gain in the tangent modulus from isotropic and kinematic hardening outweighs the loss from the  $D_{\infty}$  term.

Constraint  $\hat{g}$  defined in Eq. (25) is still challenging to impose due to its dependency on  $\varepsilon_{eq}^p$ . Two relatively simple constraints that do not depend on  $\varepsilon_{eq}^p$  are developed through an additional assumption that a>b is placed on the isotropic hardening rate parameters. The assumption a>b implies that the reduction in the yield surface associated with the  $D_{\infty}$  term occurs faster than the increase in the yield surface due to cyclic hardening associated with  $Q_{\infty}$ . This realization is supported by tests on mild steel coupons and is implied by the behavior shown in Fig. 3. The relation a>b is not directly imposed as a constraint to keep the UVC model for more general applications (e.g., for materials exhibiting cyclic softening); however, the calibration results, shown subsequently, verify this assumption. The two constraints are now presented, and afterward, they are proven to provide a nonsoftening response regardless of the applied loading.

Constraints proposed in Eqs. (26) and (27) are sufficient to ensure hardening of the material for all feasible strain histories

$$g_1 = \hat{g}|_{\varepsilon_{eq}^p = 0} = -Q_{\infty}b - \sum_k (C_k) + D_{\infty}a \le 0$$
 (26)

$$g_2 = \frac{\partial \hat{g}}{\partial \varepsilon_{eq}^p} \Big|_{\varepsilon_{eq}^p = 0} = Q_{\infty} b^2 + \sum_k (C_k \gamma_k) - D_{\infty} a^2 \le 0$$
 (27)

Note that the constraints  $g_1$  and  $g_2$  are defined in their standard form (i.e.,  $g \le 0$ ) to be compatible with standard optimization algorithms in anticipation of the calibration procedure to follow. Constraint  $g_1$  ensures that  $C_u^{ep} \ge 0$  when  $\varepsilon_{eq}^p = 0$ , and constraint  $g_2$  ensures that  $\partial C_u^{ep}/\partial \varepsilon_{eq}^p \ge 0$  when  $\varepsilon_{eq}^p = 0$ . These constraints are interpreted to mean that  $g_1$  ensures that the initial tangent modulus is nonnegative, and  $g_2$  ensures that the tangent modulus is initially increasing.

A rigorous evaluation of  $g_1$  and  $g_2$  follows two arguments based on the relationship between the magnitude of the rate parameter a to the rate parameters  $\gamma_k$ . In what follows, a > b is always assumed to reduce the number of possible minima to  $C_u^{ep}$  (Hartloper et al. 2019). The first argument is based on the assumption that  $a \ge \max \gamma_k$ . In this case, it can be shown that there is one root to  $C_u^{ep}$ , and it is a local maximum of Eq. (21) (Hartloper et al. 2019). Therefore, the minimum of  $C_u^{ep}$  occurs as  $\varepsilon_{eq}^p \to \infty$ ; however, because  $C_u^{ep} \to 0$  as  $\varepsilon_{eq}^p \to \infty$ , the tangent modulus is always nonnegative. Accordingly, if  $C_u^{ep} \ge 0$  when  $\varepsilon_{eq}^p = 0$ , the material is always nonsoftening when  $a \ge \max \gamma_k$ .

The second argument is based on the assumption that  $a < \max \gamma_k$ . In this case, there are either zero or two roots to  $C_u^{ep}$  (Hartloper et al. 2019). For zero roots,  $C_u^{ep} > 0$  for all  $\varepsilon_{eq}^p > 0$ . For two roots, it can be shown that the minimum occurs at a plastic strain less than the maximum, i.e.,  $\varepsilon_{r,\min} < \varepsilon_{r,\max}$ , where  $C_u^{ep}$  takes the local minimum and maximum values at  $\varepsilon_{r,\min}$  and  $\varepsilon_{r,\max}$ , respectively. The minimum is avoided for physically permissible values of  $\varepsilon_{eq}^p$  if the slope of the tangent modulus,  $\partial C_u^{ep}/\partial \varepsilon_{eq}^p$ , is initially greater than zero. This result follows from Eq. (6) because  $\varepsilon_{eq}^p \geq 0$  by definition. Therefore, if  $C_u^{ep} > 0$  and  $\partial C_u^{ep}/\partial \varepsilon_{eq}^p > 0$  when  $\varepsilon_{eq}^p = 0$ , the material is always hardening when  $a < \max \gamma_k$ .

The preceding arguments prove that constraints  $g_1$  and  $g_2$  ensure nonsoftening for monotonic uniaxial loading. Because monotonic loading gives the lower-bound of  $C_u^{ep}$ , we conclude that these constraints ensure nonsoftening for all uniaxial load histories. The specification of these two constraints is only possible if the parameters  $D_{\infty}$  and a are added to the original Voce-Chaboche model; otherwise, more than two roots to  $\partial C_u^{ep}/\partial \varepsilon_{eq}^p$  may exist. Constraints  $g_1$  and  $g_2$  will subsequently be used in the identification of material parameters based on uniaxial coupon tests.

#### **Multiaxial Loading**

Uniaxial results are extended for multiaxial loading based on the classical uniqueness of the elastoplastic initial boundary value problem. The condition for uniqueness in Eq. (28) is that the second-order work density is nonnegative (Simo and Hughes 1998)

$$\dot{\boldsymbol{\sigma}}:\dot{\boldsymbol{\varepsilon}} = \dot{\boldsymbol{\varepsilon}}:\mathbf{C}^{ep}:\dot{\boldsymbol{\varepsilon}} \ge 0 \tag{28}$$

where  $\mathbf{C}^{ep}$  = fourth-order tensor of *continuum* elastoplastic tangent moduli. The uniaxial interpretation of Eq. (28) to be true for all strain histories is that  $C_u^{ep} \geq 0$  (i.e., nonsoftening), and for multi-axial loading, the tensor of elastoplastic tangent moduli is positive semidefinite. We now make use of the property that positive semi-definite matrices have nonnegative eigenvalues to show that Eq. (28) is satisfied for multiaxial loading.

Neilsen and Schreyer (1993) provide two key results. First, the minimum eigenvalue of  $\mathbf{C}^{ep}$  does not depend on the direction of loading for a von Mises yield condition and an associative flow rule. Second, that the sign of the minimum eigenvalue of  $\mathbf{C}^{ep}$  is equal to the sign of the combined hardening modulus (i.e., the sum of kinematic and isotropic moduli). Therefore,  $K'_u + H'_u \ge 0$  implies that  $\mathbf{C}^{ep}$  is positive semidefinite for the proposed material model because the minimum eigenvalue is nonnegative. Therefore, nonsoftening in the uniaxial stress state enforced by the constraints defined in Eqs. (26) and (27) also enforces the uniqueness condition in Eq. (28) for multiaxial loading.

# **Calibration of Material Model Parameters**

# Methodology

Model parameters are ideally calibrated from several markedly different load protocols for material models to be representative of a material response under random strain histories. The inverse problem of determining the model parameters is stated as a constrained minimization in which the objective is to minimize the difference between the material model prediction and the test data, and the constraints impose that the material model is at no point softening. A gradient-based optimization approach using algorithmic differentiation is found to be most effective for similar problems (de Castro e Sousa et al. 2020); therefore, a similar strategy is utilized in this study.

The minimization problem to be solved is defined in Eq. (29)

$$\underset{x \in \mathbb{R}^n}{\text{minimize}} \quad f(x) \tag{29a}$$

subject to 
$$g(x) \le 0$$
 (29b)

where  $\mathbf{x} = [E, \sigma_{y,0}, Q_{\infty}, b, D_{\infty}, a, C_1, \gamma_1, \dots, C_{N_k}, \gamma_{N_k}]$  is the vector of n parameters for the UVC model under uniaxial loading;  $f(\mathbf{x}):\mathbb{R}^n \to \mathbb{R}$  is the objective function; and  $\mathbf{g}(\mathbf{x}):\mathbb{R}^n \to \mathbb{R}^m$  is a vector-valued function of constraints (i.e., there are m constraints defined). The goal of the proposed calibration procedure is to find

the set of material parameters x that is a local minimum of the objective function and satisfy the nonsoftening constraints.

The objective function defined in Eq. (30) is in keeping with the definition by de Castro e Sousa et al. (2020)

$$f(\mathbf{x}) = \sum_{j=1}^{N_T} \frac{\int_0^{\varepsilon_j^*} (\sigma_j^{\text{model}}(\varepsilon_j; \mathbf{x}) - \sigma_j^{\text{test}})^2 d\epsilon^*}{\int_0^{\varepsilon_j^*} d\epsilon^*}$$
(30)

where  $N_T$  load histories are considered;  $\sigma_j^{\text{model}}(\varepsilon_j; \mathbf{x}) = \text{stress}$  from the UVC model given strain history  $\varepsilon_j$  and parameters  $\mathbf{x}$ ;  $\sigma_j^{\text{test}} = \text{stress}$  recorded in the uniaxial test j; and  $\varepsilon^* = \text{accumulated}$  strain

$$\varepsilon_j^* = \int_0^{t_j} |\dot{\varepsilon}_j| d\tau \tag{31}$$

The objective function f(x) represents the total squared-area between the model prediction and test data normalized by the total accumulated strain for several tests [see the shaded region in Fig. 1(b) for a single test]. Constraints to impose nonsoftening are considered for the proposed model,  $g(x) = [g_1, g_2]$ , defined by Eqs. (26) and (27). The parameter space is further limited to x > 0 to obtain physically meaningful results and to ensure convergence of the return mapping algorithm.

Eq. (29a) is solved in multiple steps because it is challenging to obtain a solution due to the nonlinearity of the constraints and the indefiniteness of the Hessian of f(x) (de Castro e Sousa et al. 2020). Numerical testing reveals that solving the problem of Eq. (29a) subjected to Eq. (29b) directly is not practical and that the solution time can be significantly reduced by using an appropriate starting point (Hartloper et al. 2019). The first step is to solve Eq. (29a) using the Voce-Chaboche model (i.e., without  $D_{\infty}$  and a) following the methodology by de Castro e Sousa et al. (2020). The starting point to the Voce-Chaboche model is chosen as a perfectly plastic material with nominal elastic modulus and initial yield stress. All hardening parameters are initially set to  $10^{-1}$  to represent the perfectly plastic conditions. Once the solution point using the Voce-Chaboche model has been found, the added parameters that constitute the UVC model are set to  $D_{\infty}=10^{-1}$  and a=200, and this point is denoted as  $x_{ini}$ . The choice of a is made on the observation that the Luders strain is typically around a 2% strain for mild steels, corresponding to  $a \approx 230$  for a 99% saturation

The second step is to solve Eq. (29a) subjected to Eq. (29b) with the UVC model starting from  $\boldsymbol{x}_{ini}$  using the nonlinear interior-point trust-region optimizer (NITRO) algorithm described by Byrd et al. (1999) and implemented in the Python package Scipy (Jones et al. 2001). The NITRO algorithm is found to be the most efficient when compared to the alternative constrained trust-region (Conn et al. 2000; Bierlaire 2015) and sequential quadratic programming methods (Bierlaire 2015). An additional benefit of this algorithm is that solution points can be found starting from infeasible starting points. Solution points are defined by the local minima of the objective function. Minima are defined by the first-order necessary condition

$$\|\nabla f(\mathbf{x})\| < \epsilon_{\text{tol}} \tag{32}$$

and the second-order necessary condition that the Hessian of f(x) is positive definite. The symbol  $\nabla(\cdot)$  in Eq. (32) is the gradient operator, and the tolerance is initially defined as  $\epsilon_{\rm tol}=10^{-8}$ . Even starting from  $x_{ini}$ , obtaining a solution to Eq. (29) to  $10^{-8}$  is challenging due to the aforementioned nonconvexity of the objective function and nonlinearity of the constraints. Experience shows that satisfactory solutions can be found by successively relaxing the tolerance from  $10^{-8}$  to  $10^{-2}$  after 300 iterations and then finally to

 $5 \times 10^{-2}$  after a further 1,000 iterations. The aforementioned calibration procedure is implemented in the open-source Python package RESSPyLab (de Castro e Sousa et al. 2019).

# Summary of Results for Structural Steel Materials

#### **Definition of Metrics**

Metrics are defined to quantify the model fit and hardening characteristics of each steel material. The quality of fit is defined by the  $\bar{\varphi}$  metric in Eq. (33) that represents the model error normalized by the total squared-area under all the stress-strain curves in the data set

$$\bar{\varphi} = \sqrt{f(\mathbf{x}) \times \left(\sum_{j=1}^{N_T} \frac{\int_0^{\varepsilon_j^*} (\sigma_j^{\text{test}})^2 d\epsilon^*}{\int_0^{\varepsilon_j^*} d\epsilon^*}\right)^{-1}}$$
(33)

A value of  $\bar{\varphi}=0$  indicates a perfect fit, and increasing values indicate decreasing qualities of fit.

The following metrics are defined in terms of the equivalent plastic strain assuming monotonic loading for a fixed set of parameters. The total increase in stress due to hardening is described by the metric in Eq. (34)

$$\sigma_{\text{hard}}(\varepsilon_{eq}^{p}) = Q_{\infty}(1 - \exp[-b\varepsilon_{eq}^{p}]) + \sum_{k} C_{k}/\gamma_{k}(1 - \exp[-\gamma_{k}\varepsilon_{eq}^{p}])$$
(34)

The ratios of isotropic and kinematic contributions to the total hardening are respectively defined by the metrics in Eqs. (35) and (36)

$$\rho_{\rm iso}(\varepsilon_{eq}^p) = \frac{Q_{\infty}(1 - \exp[-b\varepsilon_{eq}^p])}{\sigma_{\rm hard}(\varepsilon_{eq}^p)}$$
(35)

$$\rho_{\rm kin}(\varepsilon_{eq}^p) = \frac{\sum_k C_k / \gamma_k (1 - \exp[-\gamma_k \varepsilon_{eq}^p])}{\sigma_{\rm hard}(\varepsilon_{eq}^p)}$$
(36)

A value of  $\rho_{\rm kin}=1$  ( $\rho_{\rm iso}=0$ ) indicates that there is only kinematic hardening present in the material. The total stress at a particular value of  $\varepsilon_{eq}^p$  is defined by Eq. (37)

$$\sigma_{\text{total}}(\varepsilon_{eq}^p) = \sigma_{\text{v},0} + \sigma_{\text{hard}}(\varepsilon_{eq}^p) - D_{\infty}(1 - \exp[-a\varepsilon_{eq}^p])$$
 (37)

and the ratio of stress at saturation to the initial yield stress is given in Eq. (38)

$$\rho_{\text{yield}}(\varepsilon_{eq}^p) = \frac{\sigma_{\text{total}}(\varepsilon_{eq}^p)}{\sigma_{y,0}} \tag{38}$$

A value of  $\rho_{\text{yield}} = 2$  would indicate that the stress at the chosen value of  $\varepsilon_{eq}^p$  is twice the initial yield stress.

All the preceding metrics can be evaluated at any particular  $\varepsilon^p_{eq}$  value. The choice of saturation (i.e.,  $\varepsilon^p_{eq} \to \infty$ ), indicated by the "sat" superscript, is made for convenience and to compare with de Castro e Sousa et al. (2020). However, the choice of  $\varepsilon^p_{eq} \approx 0.15$  could be more representative of the ultimate material behavior.

#### **Results and Discussion**

Parameters for the UVC model based on 12 sets of coupon tests on mild structural steels from Europe, North America, and Japan are provided and evaluated in this section. Nine steel materials are included in this database. These steels can be classified as either carbon structural steels (e.g., S355J2+N, A992 Gr. 50, A500 Gr. B, BCP325, and BCR295) or high-strength low-alloy structural steels (e.g., S460NL and S690QL), according to ASTM (2018). The high

Table 1. Summary of steel material database and metrics for the proposed material model

ID	Material	$f_{y,n}$ (MPa)	Reference	LP	$\bar{\varphi}$ (%)	$\sigma_{\mathrm{total}}^{\mathrm{sat}}$ (MPa)	$\sigma_{\rm hard}^{\rm sat}$ (MPa)	$ ho_{ ext{yield}}^{ ext{sat}}$	$ ho_{ m iso}^{ m sat}$	$ ho_{ m kin}^{ m sat}$
1	S355J2+N 50 mm plate	355	1	1–10	6.33	701.93	462.91	2.11	0.26	0.74
2	S355J2+N 25 mm plate	355	1	1-10	6.53	681.02	475.97	2.01	0.28	0.72
3	S355J2 HEB500 flange	355	3	1,2,5,6,9	3.96	636.59	417.72	2.02	0.33	0.67
4	S355J2 HEB500 web	355	3	1,1-3,5-9	5.65	548.55	333.94	1.64	0.42	0.58
5	S460NL 25 mm plate	460	1	1,3-7,9,10	5.46	818.32	515.76	1.86	0.19	0.81
6	S690QL 25 mm plate	690	1	1,3-7,9,10	6.20	896.50	343.41	1.31	0.00	1.00
7	A992 Gr.50 W14X82 web	345	2	1,2,5,6,9	5.21	643.27	407.93	1.70	0.30	0.70
8	A992 Gr.50 W14X82 flange	345	2	1,2,5,6,9	4.76	786.49	548.72	2.10	0.26	0.74
9	A500 Gr.B HSS305X16	315	2	1,2,5,6,9	4.99	832.57	558.90	2.57	0.41	0.59
10	BCP325 22 mm plate	325	2	1,2,5,6,9	3.89	662.04	399.96	1.80	0.28	0.72
11	BCR295 HSS350X22	295	2	1,2,5,6,9	5.21	996.09	687.18	2.42	0.00	1.00
12	HYP400 27 mm plate	400	2	1,2,5,6,9	4.67	797.99	452.81	1.76	0.14	0.86

Note: Steels 1–6 are European, 7–9 are North American, and 10–12 are Japanese; HSS = hollow structural section;  $f_{y,n}$  = nominal yield stress; and LP = load protocols tested. See de Castro e Sousa et al. (2020) for definitions. Reference 1 refers to the study by Grigoriou and Lignos (2017), Reference 2 refers to that by Suzuki (2018), and Reference 3 was conducted as a part of this study.

**Table 2.** Proposed material model parameters for structural steels

ID	E (GPa)	$\sigma_{y,0}$ (MPa)	$Q_{\infty}$ (MPa)	b	$D_{\infty}$ (MPa)	а	$C_1$ (MPa)	$\gamma_1$	$C_2$ (MPa)	$\gamma_2$
1	185.97	332.18	120.48	8.14	93.15	261.75	21,102.00	173.60	2,300.60	10.42
2	197.41	338.80	134.34	14.71	133.75	229.25	26,242.00	199.04	2,445.30	11.66
3	192.13	315.04	138.01	11.36	96.16	223.66	18,587.84	257.31	1,351.98	6.52
4	199.68	334.94	139.32	14.07	120.33	274.73	28,528.03	315.17	2,569.45	24.68
5	187.61	439.20	97.35	14.02	136.64	226.40	26,691.00	188.75	2,892.40	10.44
6	188.63	685.39	0.11	0.11	132.30	285.15	34,575.00	185.16	3,154.20	20.14
7	210.74	378.83	122.63	19.74	143.49	248.14	31,638.00	277.32	1,548.60	9.04
8	191.02	373.72	141.47	15.20	135.95	211.16	25,621.00	235.12	942.18	3.16
9	191.21	324.09	228.02	0.11	50.41	270.40	17,707.00	207.18	1,526.20	6.22
10	178.61	368.03	112.25	10.78	105.95	221.92	20,104.00	200.43	2,203.00	11.76
11	178.74	412.21	0.09	0.09	103.30	212.83	20,750.59	225.26	1,245.04	2.09
12	189.36	454.46	62.63	16.57	109.28	145.74	13,860.00	141.61	1,031.10	3.53

Note: ID column corresponds to Table 1.

yield point (HYP) steel is a mild steel for structural applications in which the yield stress is enhanced through a thermomechanical control process and grain refinement (Suzuki et al. 2008; Kanno 2016; Suzuki 2018). The steel material type, nominal yield stress, load protocols used for calibration, and evaluation metrics for all the data sets are summarized in Table 1. Up to 10 different strain-based load protocols deemed to be representative of strain histories in steel components subjected to earthquake loading are utilized for each material based on the suggestion by Suzuki (2018). Definitions for the load protocols are found in the study by de Castro e Sousa et al. (2020).

Parameters for the 12 data sets are provided in Table 2; note that the identification (ID) number for all the steel materials in this table are in correspondence with Table 1. Table 3 collects the yield stress measured using the 0.2% offset method for each dataset (averaged over all tests in each set), along with the  $\sigma_{y,0}$  values and error metric values  $\bar{\varphi}$  for the Voce-Chaboche and UVC models. This table shows that the UVC  $\sigma_{y,0}$  is only 4% different from the average measured yield stress, while the Voce-Chaboche  $\sigma_{y,0}$  is 17% different from the average measured yield stress. A 4% difference in the initial yield stress is notably accurate, especially considering the discontinuous nature of the stress in the plateau region measured by the 0.2% offset method. Furthermore, the UVC model leads to a relative reduction in the normalized error metric by about 20% on average compared to the Voce-Chaboche model.

The proposed UVC material model provides a better fit of the test data and a better estimation of the initial yield stress and also

better approximates the initial plateau found in mild carbon steels when compared with the Voce-Chaboche model. Several key points are now highlighted using the Voce-Chaboche model parameters from 10 of the same data sets in the study by de Castro e Sousa et al. (2020) as a basis for comparison. The goodness-of-fit for all the load histories considered is shown in Figs. 8 and 9 for data sets from the flange and web of an HEB500 section that were tested as a part of the current study (IDs 3 and 4 in Table 1). In each of these figures, VC is the Voce-Chaboche model prediction. Results from two data sets are shown in this study for brevity, but comparisons of the remaining data sets are provided in the study by Hartloper et al. (2019). Although differences between the original and updated models may seem entirely insignificant, in all these figures, notice that the plateau yield stress is closely predicted by the updated material model, whereas the same is not true for the original model. A case study subsequently demonstrates that there is a significant impact on the prediction of wide-flange column postpeak behavior despite the closeness between the two material predictions.

Values of the ratio of isotropic-to-total hardening,  $\rho_{\rm iso}^{\rm sat}$ , in Table 1 show that mild carbon structural steels have a higher ratio of isotropic hardening than the high-strength low-alloy steels. The  $\rho_{\rm iso}^{\rm sat}$  metric is around 25%–40% for the mild carbon structural steels (e.g., S355J2+N, A992 Gr. 50) and is negligible for high-strength steels (e.g.,  $\rho_{\rm iso}^{\rm sat}=0$  for S690QL). One exception to this observation is the BCR295 data set that does not exhibit cyclic hardening because the coupons were sampled from the corners of a

Table 3. Comparison of yield stresses and normalized error metrics for the UVC and Voce-Chaboche (VC) models

ID	$f_{ym,a}$ (MPa)	$\sigma^{UVC}_{y,0}$ (MPa)	$\sigma^{VC}_{y,0}$ (MPa)	Error, $f_y$ UVC (%)	Error, $f_y$ VC (%)	$\bar{\varphi}^{UVC}$ (%)	$\bar{\varphi}^{VC}~(\%)$	Error, $\bar{\varphi}$ (%)
1	339	332	271	2	18	6.33	6.37	
2	358	339	265	5	22	6.53	6.70	-3
3	305	315	246	3	22	3.96	4.63	-14
4	350	335	252	4	25	5.65	6.16	-8
5	446	439	359	1	18	5.46	6.32	-14
6	714	685	603	4	12	6.20	7.95	-22
7	386	379	339	2	10	5.21	7.01	-26
8	393	374	318	5	15	4.76	7.31	-35
9	343	324	301	6	7	4.99	6.86	-27
10	380	368	306	3	17	3.89	5.05	-23
11	392	412	346	5	16	5.21	8.38	-38
12	463	454	376	2	17	4.67	5.31	-12
Average	_	_	_	4	17	_	_	-19

Note:  $f_{ym,a} = \text{average yield stress for each data set}; \ \sigma^{VC}_{y,0} \ \text{and} \ \bar{\varphi} \ \text{are taken from the study by de Castro e Sousa et al. (2020); Error,} \ f_y \, \text{UVC} = |\sigma^{UVC}_{y,0} - f_{ym,a}|/f_{ym,a}; \, \text{Error,} \ f_y \, \text{VC} = |\sigma^{VC}_{y,0} - f_{ym,a}|/f_{ym,a}; \, \text{and Error,} \ \bar{\varphi} = (\bar{\varphi}^{UVC} - \bar{\varphi}^{VC})/\bar{\varphi}^{VC}.$ 

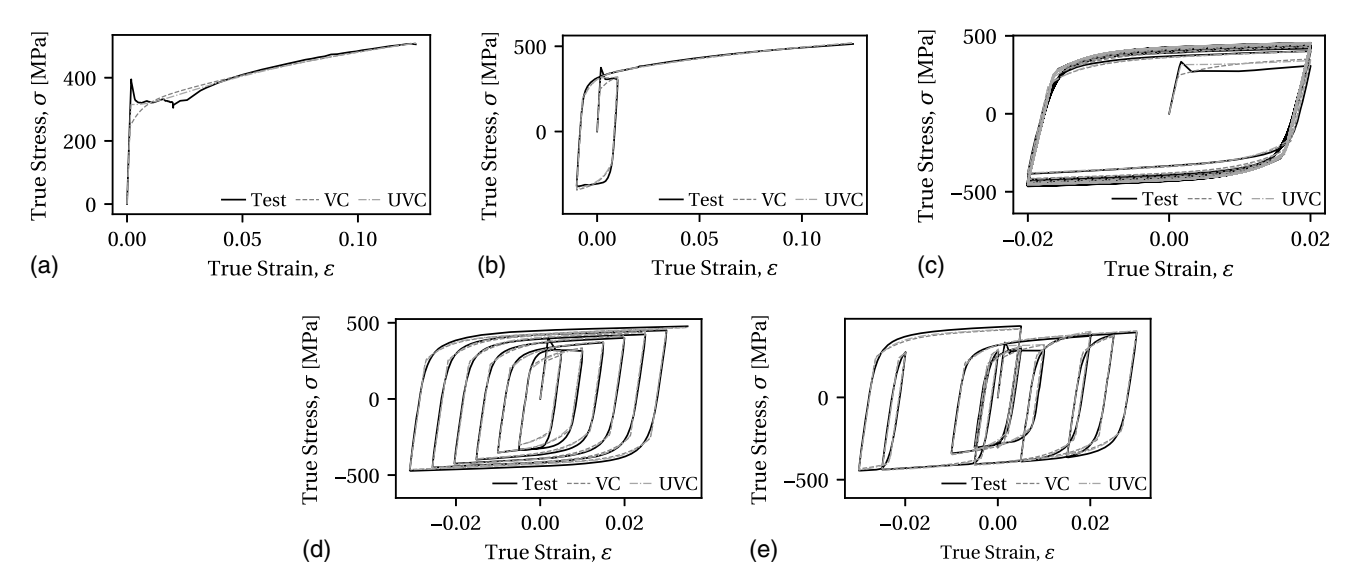


Fig. 8. Comparison of test data and model predictions for the S355J2 HEB500 flange data set: (a) LP 1; (b) LP 2; (c) LP 5; (d) LP 6; and (e) LP 9.

cold-pressed hollow structural section. Recalling that isotropic hardening is a reflection of the amount of cyclic hardening exhibited by the physical material, these results suggest that high-strength steels do not exhibit much cyclic hardening. This finding is in agreement with that of de Castro e Sousa et al. (2020) for the original Voce-Chaboche model and is visually confirmed by the plots of stress-strain data for the S690QL steel (Hartloper et al. 2019).

Comparing the UVC and Voce-Chaboche models, there is a larger portion of isotropic hardening in the updated model, and the total stress at saturation is similar. The value of  $\rho_{\rm iso}^{\rm sat}$  varies between 20% and 25% for S355J2+N and A992 Gr. 50 steels in the study by de Castro e Sousa et al. (2020) for the Voce-Chaboche model. Ratios of isotropic-to-kinematic hardening tend to be higher in the UVC model because  $Q_{\infty}$  is increased to compensate for the negative effect of  $D_{\infty}$ . Comparing  $\sigma_{\rm total}^{\rm sat}$  from Table 1 with their equivalent values in the study by de Castro e Sousa et al. (2020), there is an average of a 1% difference between the two models across all the comparable material data sets. These two results suggest that although the composition of total hardening is different between the two models, the ultimate stress at saturation is comparable.

A reduction in the yield surface is observed in all of the evaluated materials, and the magnitude of  $Q_{\infty}$  seems to be roughly equal

to that of  $D_{\infty}$  for the carbon steels (apart from BCR295 due to cold working). Isotropic hardening parameter  $Q_{\infty}$  is greater than  $D_{\infty}$  in 7 out of the 12 data sets for the updated material model. These results imply that the decrease in the yield surface due to discontinuous yielding is roughly balanced by the increase due to cyclic hardening. The magnitude of  $D_{\infty}$  is itself significant for all the data sets, indicating that there is some reduction in the yield surface even in high strength steels, e.g., S690QL steel. Although this material does not visually exhibit discontinuous yielding or cyclic hardening (i.e.,  $Q_{\infty} \approx 0$ ), the fact that  $D_{\infty} > 0$  suggests that interstitial impurities may still play a role in restricting dislocation movement that diminishes with increasing accumulated plastic strain. Applications of the proposed material model to other steels that contain a reduction in the yield surface, e.g., due to cyclic softening, is left for future investigations.

# Note on the Number of Backstresses

At least two backstresses are necessary to adequately model the kinematic hardening observed in mild steels using the UVC model. One backstress is found to be insufficient to represent the kinematic hardening, leading to irrational estimates of other parameters

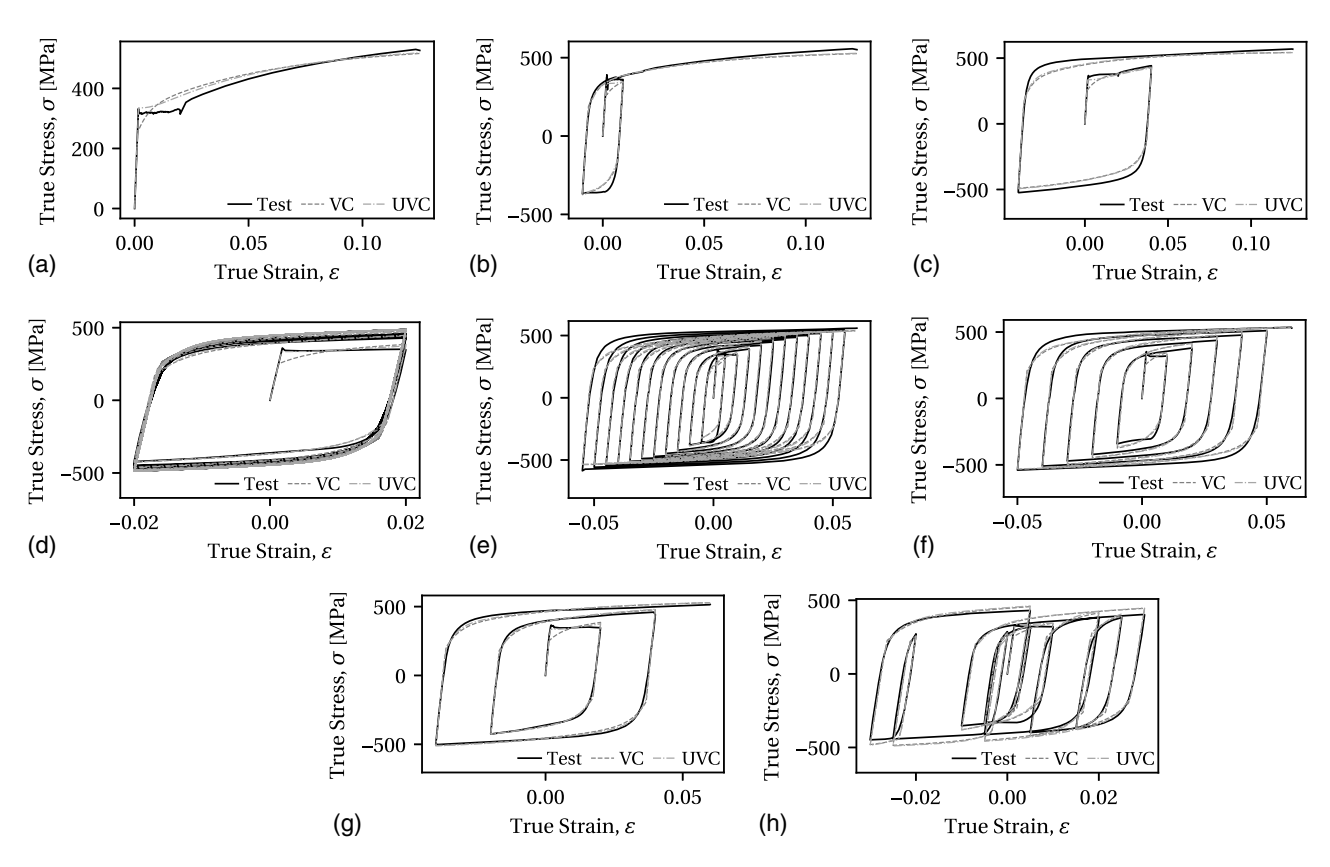


Fig. 9. Comparison of test data and model predictions for the S355J2 HEB500 web data set: (a) LP 1; (b) LP 2; (c) LP 3; (d) LP 5; (e) LP 6; (f) LP 7; (g) LP 8; and (h) LP 9.

(Hartloper et al. 2019). There is little improvement in  $\bar{\varphi}$  when three backstresses are used, echoing the results from de Castro e Sousa et al. (2020) for the original Voce-Chaboche model. Therefore, two backstresses provide an optimal mix of accuracy and efficiency while adequately representing the kinematic hardening observed in the test data.

# Finite-Element Analysis Case Study and Implications

The sensitivity of CFE models to their initial material model assumptions is explored in this section through a parametric study. The evaluation is established by comparing the response of two-column models with identical geometric characteristics: one using the Voce-Chaboche model and the other with the UVC model. Variations in the material model parameters, as well as the imperfections, are considered in this study to conclude whether the differences

Table 4. Cross-section properties of an HEB500, 7,000 mm length

Properties	Values
$A \text{ (mm}^2)$	23,900
h (mm)	500
b (mm)	300
$t_w$ (mm)	14.5
$t_f$ (mm)	28
$h_1/t_w$	26.9
$b/2t_f$	5.4
$L_b/\widetilde{i_z}$	72.7
$rac{L_b/\dot{i}_z}{ar{\lambda}_{LT}}$	1.0

in the observed behavior consistently arise between simulations carried out with the two material models.

The parametric study focuses on the simulated performance of an HEB500 cross-section (similar to a W610X217, or W24X146 in North America) of a 7,000-mm length subjected to multiaxis loading. Relevant geometric characteristics of this column are provided in Table 4. In this table, A is the cross-sectional area, h is the section depth, b is the flange width,  $t_w$  is the web thickness,  $t_f$  is the flange thickness,  $h_1$  is the clear distance between flanges,  $L_b$  is the column unbraced length,  $i_z$  is the radius of gyration in the weak axis, and  $\bar{\lambda}_{LT}$  is the lateral-torsional buckling slenderness calculated according to Eurocode (CEN 2005a). This cross-section satisfies the Eurocode Class 1 criteria for the applied compression and bending (CEN 2005a) and the AISC highly ductile classification criteria (AISC 2016). However, the column has relatively large member slenderness, indicated by its  $L_b/i_z$  value, and is susceptible to lateral-torsional buckling (LTB) coupled with plastic local buckling because Eurocode indicates that inelastic LTB should occur when  $0.4 < \bar{\lambda}_{LT} < 1.2$ .

# Modeling Procedure

Column models for the HEB500 column are developed following the guidelines by Elkady and Lignos (2018b) using the software Abaqus v6.14 (ABAQUS 2014). The adequacy of these guidelines for similar cross-sections has been established through validations with several columns (Elkady and Lignos 2018b) and success by the first and third authors in winning a recent blind analysis competition (ATC 2018). The models are comprised of quadrilateral reduced integration shell elements (S4R) with a mesh size of approximately 25 mm. Residual stresses are considered in the model based on the Young (1972) stress distribution because de Castro e

Table 5. Original Voce-Chaboche model parameters for the case study material sets

Material	E (GPa)	$\sigma_{y,0}$ (MPa)	$Q_{\infty}$ (MPa)	b	$C_1$ (MPa)	$\gamma_1$	$C_2$ (MPa)	$\gamma_2$
S355J2 HEB500 flange S355J2 HEB500 web	191.85 198.39	245.50 251.74	119.77 118.43	8.67 10.85	14,019.86 17,876.51	205.39 236.30	1,247.05 2,582.61	4.45 24.01
S355J2+N 25 mm plate	191.52	265.29	104.44	11.63	12,997.99	99.52	1,560.41	7.35

Sousa and Lignos (2017) suggests that this distribution is adequate for HEB500 cross-sections.

Two material data sets are chosen to be consistent with the HEB500 cross-section. Parameters constituting Material set 1 are chosen as the S355J2+N 25 mm plate data set because the plate thickness best matches the flange and web thickness of the HEB500 section given the existing data. Material set 2 is based on material tests conducted as a part of the present study using 12- and 20-mm diameter round bar coupons (with a diameter in the reduced section of 6 and 10 mm, respectively) from the web and flange of an HEB500. A second set of parameters is used to establish confidence that the results of this case study hold for multiple data sets. Material parameters for the Voce-Chaboche model are provided in Table 5 using the procedure by de Castro e Sousa et al. (2020), and parameters for the UVC model are taken from Table 2.

Loading and boundary conditions on the column models are shown in Fig. 10(a). Rigid-body constraints are applied to the nodes at the top and base of the CFE models to avoid stress concentrations in these regions; all loads and boundary conditions are then applied at the centroid of the cross-section. Fixed-end boundary conditions are assumed, and the same constant compressive axial load is applied to all models based on 20% of the axial load at first yield,  $A\sigma_{v,0}$ , where A is the nominal area, and  $\sigma_{v,0}$  is taken as the value from the updated material model for the S355J2+N 25 mm plate data set from Table 2. The symmetric cyclic lateral displacement history from Chapter K of AISC (2016) is applied at the column top after the application of the gravity load, as depicted in Fig. 10(a). Default convergence criteria in Abaqus v6.14 is used with automatic time-stepping; however, outputs are generated at the exact same analysis times to make the analyses as comparable as possible.

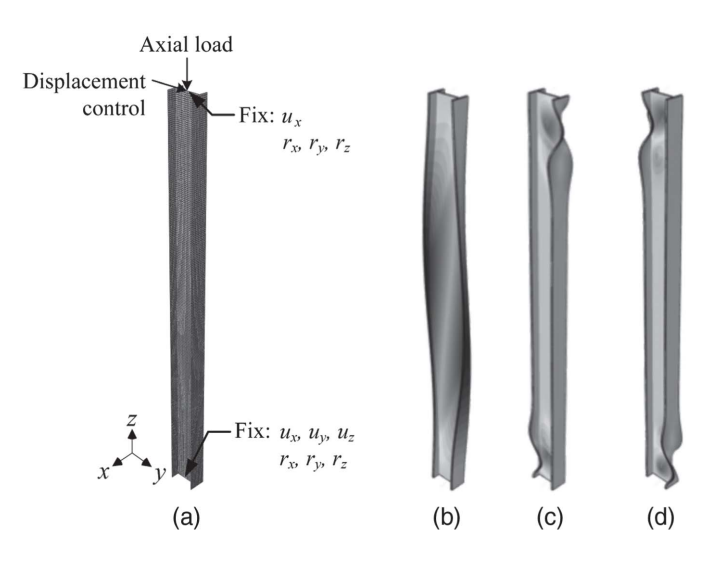


**Fig. 10.** Continuum finite-element model and elastic buckling modes for the HEB500 column case study: (a) CFE model; (b) Mode 1; (c) Mode 5; and (d) Mode 6.

#### Geometric Imperfections

Geometric imperfections are included to induce LTB and local buckling by scaling and superimposing relevant elastic buckling modes (Elkady and Lignos 2018b). These geometric imperfections are determined by first applying the axial load and then applying a lateral force and conducting an elastic eigenvalue buckling analysis in Abaqus. Modes 1 and 2 correspond to LTB, and Modes 5 and 6 corresponding to local buckling are visually selected. Modes 1, 5, and 6 are shown in Fig. 10—note that Mode 2 is simply the inverse of Mode 1. Both Modes 1 and 2 are applied independently to the model to consider the random nature of imperfections that could induce LTB in either of the two directions.

For the purpose of this parametric study, geometric imperfections with amplitudes below the manufacturing limits, e.g., CEN (1993), are applied to the column models. The imperfection amplitudes are based on the mean and standard deviation of previously measured imperfections. Five scale factors are considered for both the LTB and local buckling modes,  $a_{\mu}$ ,  $a_{\mu\pm\sigma}$ , and  $a_{\mu\pm\sigma/2}$ , where a is the scale factor, and subscripts  $\mu$  and  $\sigma$  denote the mean standard deviation of the measurements, respectively. The derivation of the imperfection scale factors is now discussed.

Twist measurements from 10 full-scale steel columns featuring cross-sections similar to the present study are used to deduce the LTB imperfections scale factors (Elkady 2016; Elkady and Lignos 2018a). LTB imperfection scale factors are related to the measured angles of twist through Eq. (39)

$$a^{\rm LTB} = \frac{\theta_{\rm applied}}{\theta_{\rm ref}} \tag{39}$$

where  $a^{\rm LTB}$  = scale factor applied to Modes 1 or 2;  $\theta_{\rm applied}$  = intended rotation at column midheight based on the measured imperfections; and  $\theta_{\rm ref}$  = estimate of the midheight rotation for Modes 1 and 2 from the buckling analysis. Note that Elkady (2016) recorded the initial rotational imperfection at the column top; therefore, the values at midheight are assumed to be one-half of the values reported at the top. The reference twist angle corresponding to the imperfections in Modes 1 and 2 are deduced using Eq. (40) based on the rotation of the web about its centerline

$$\theta_{\text{ref}} = \arcsin\left[\frac{2u_w}{h - t_f}\right] = 0.004 \text{ rad} \tag{40}$$

where  $u_w$  = displacement of the web from the HEB500 model at midheight due to buckling Mode 1. Eq. (40) is evaluated, considering that  $u_w \approx 1.0$  mm due to the normalization of buckling modes in Abaqus. The mean twist for the LTB imperfection is calculated as 0.006 rad, and the standard deviation is 0.005 rad (Elkady 2016). The scale factors for the LTB imperfections based on the mean and standard deviation using Eq. (39) are provided in Table 6.

Measurements from six European steel wide-flange sections are used to deduce the local imperfection scale factors. Local imperfection scale factors are related to the measured flange and web imperfections through Eq. (41)

**Table 6.** Imperfection scale factors for lateral-torsional and local buckling modes

	Basis of imperfection scale factor						
Imperfection mode	$\mu - \sigma$	$\mu - \sigma/2$	$\mu$	$\mu + \sigma/2$	$\mu + \sigma$		
Lateral-torsional buckling modes (1, 2), $a^{\text{LTB}}$	0.24	0.83	1.40	2.00	2.59		
Local buckling modes (5, 6), $a^{loc}$	0.53	0.87	1.20	1.54	1.87		

Note:  $\mu$  = mean of measurements; and  $\sigma$  = standard deviation of measurements.

$$a^{\rm loc} = \frac{\Delta_{\rm applied}}{\Delta_{\rm ref}} \tag{41}$$

where  $a^{\rm loc}$  = scale factor applied to Modes 5 and 6;  $\Delta_{\rm applied}$  = intended local imperfection amplitude; and  $\Delta_{\rm ref}$  = 1.0 mm = maximum nodal displacement from Modes 5 and 6. Hartloper and Lignos (2019) report the mean measured web imperfections amplitude as h/300 and the standard deviation as h/1,017. From the same study, the mean measured flange imperfection amplitude is h/250, and the standard deviation is h/466. The mean measured values are consistent with European manufacturing limits (CEN 1993) as well as those proposed by Elkady and Lignos (2018b). The scale factors for the local imperfections based on the mean and standard deviation using Eq. (41) are provided in Table 6.

# Parametric Study and Results

Both the material properties and geometric imperfections are varied to investigate the consistency of the divergence in buckling modes. With this parametric study, we vary the geometric imperfections within expected ranges for common steel profiles. This approach intends to show that if, for a range of variations in the geometric imperfections, there is a consistent divergence in the column behavior for different material models, then it can be reasonably concluded that the accuracy of the material model is the principal cause of the divergence. A total of 15 comparisons are conducted for each material set in which the geometric imperfection scale factors are varied equally for the columns using both the Voce-Chaboche and UVC models. Parameters from two material sets are chosen for a total of 30 comparisons. The parametric study follows three steps for Material set 1 (\$355J2+N, 25 mm plate). First, five comparisons are made using the imperfection scale factors given in Table 6, varying the LTB imperfection Mode 1 with constant local imperfection geometry. Second, five comparisons are made in a similar fashion but varying LTB Mode 2 with constant local imperfection geometry. Third, five comparisons are made varying the local imperfection scale factors for Modes 5 and 6 based on Table 6, with constant LTB imperfection Mode 1 geometry. The same three steps are then carried out using Material set 2 (S355J2 HEB500 flange and web).

Results from the parametric study indicate that while the prepeak responses of the simulations are similar, there is a consistent divergence in the simulated buckling modes between the two columns that use different material representations. A comparison of the column base moment—chord rotation for Material set 2, and all imperfections at the mean amplitude are shown in Fig. 11(a). Typical deformed shapes observed from the analyses using the Voce-Chaboche and UVC material models are shown in Figs. 11(b and c), respectively. The similarity in the prepeak responses between the two models may seem counterintuitive as the largest difference in material appears in the initial yield stress. However, the initial hardening of the Voce-Chaboche model is increased to compensate

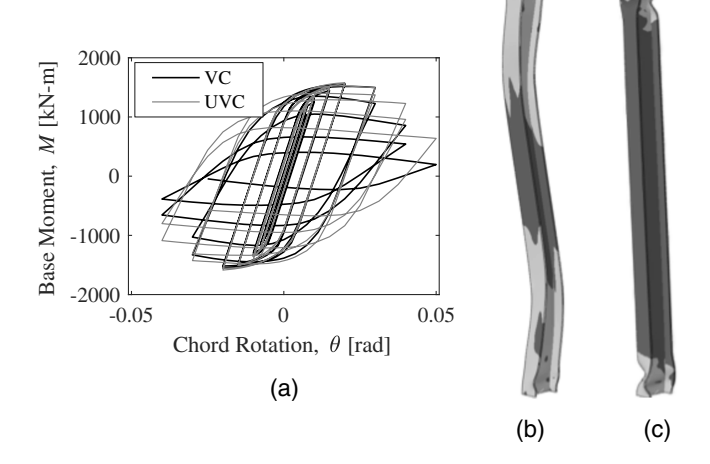


**Fig. 11.** Column base moment—chord rotation and column model deformation modes (yielding shown in light gray) at the first excursion to −4% chord rotation: (a) moment-rotation, Material set 1, mean imperfection amplitudes; (b) VC model; and (c) UVC model.

for its lower initial yield stress, so the overall prepeak component response is relatively similar. Significant differences in the component behavior only arise in this case study after strength deterioration due to buckling in the component has occurred.

Divergence in the component simulations arises primarily due to the difference in initial yield stress between the two material models. Observe in Figs. 11(b and c) that the extent of yielding along the column length from the ends, or plastic hinge length, is around three times greater when the Voce-Chaboche material model is used. Yielding is shown visually in these figures as the light gray regions. At the first excursion to -4% chord rotation, the spread of plasticity is almost up to 80% of the column half-length for the Voce-Chaboche model, whereas this value is only around 30% for the UVC model. The long plastic hinge lengths in the model with the Voce-Chaboche material significantly reduce the torsional stiffness of the column. In turn, this allows for the initiation of lateral-torsional buckling. Similar observations are made by Elkady and Lignos (2018a) with respect to full-scale wide-flange column tests.

The increased initial yield stress of the UVC model does not allow for such a long plastic hinge length to form. Lateral-torsional buckling does not occur in this case, and the deterioration in strength and stiffness is due to local buckling followed by column twisting. This case study shows that columns with relatively high member slenderness ratios (e.g.,  $L_b/i_z > 90$ ) can be sensitive to the difference in initial yield stress because these members are prone to experiencing coupled local and lateral-torsional buckling. Such components are, therefore, sensitive to the choice of material model parameters.

Consistency in the difference between simulated component responses is evaluated to assess if the aforementioned sensitivity holds for different material parameters and imperfection geometries. Results from the parametric study are compiled in Table 7 in terms of an error metric defined by Eq. (42) that measures the relative difference in a moment between the two analyses over the common load history

$$E_m = \frac{\|\mathbf{M}_{UVC} - \mathbf{M}_{VC}\|}{\|\mathbf{M}_{VC}\|} \times 100 \tag{42}$$

where M = discrete vector of the column base moment up to the last common time increment between the two analyses; and the

Table 7. Summary of the error metric from the parametric case study

	Erro	or metric (%), Material s	et 1	Erro	or metric (%), Material s	set 2
VM scale	VM1, CM56	VM2, CM56	CM1,VM56	VM1, CM56	VM2, CM56	CM1, VM56
$\mu - \sigma$	17.5	17.6	19.8	21.3	22.6	15.5
$\mu - \sigma/2$	18.7	18.8	19.6	24.5	22.6	24.2
$\mu$	19.0	18.9	19.0	23.6	25.3	23.6
$\mu + \sigma/2$	19.3	19.2	17.6	22.8	21.0	22.4
$\mu + \sigma$	19.3	19.3	6.7	21.1	20.7	16.3

Note: VM = varying mode; CM = constant mode(s), all the constant modes at mean scale factor;  $\mu$  = mean of measurements; and  $\sigma$  = standard deviation of measurements.

subscripts denote the analyses using either the Voce-Chaboche (VC) or UVC material model. In Table 7, the columns with VM indicate the imperfection modes with varied amplitude (e.g., VM1 means that the amplitude of Mode 1 is varied, and VM56 means that the amplitudes of Modes 5 and 6 are varied), and the columns with CM indicate the imperfection modes with a constant mean amplitude.

Results from the parametric study in Table 7 suggest that the difference in the base moment over the load history is up to about 20%. Values in this table of around 15%-20% are the analyses where different buckling modes are observed, while the one value of 6.7% (Material set 1,  $\mu + \sigma$  local buckling imperfection amplitude) is a case in which the same buckling modes are observed. In this specific case, the response is similar because there is a relatively large local imperfection applied that leads to primarily local buckling, even for the column model with the Voce-Chaboche material model. The majority of error metrics in Table 7 falling into the 15%-20% range, in conjunction with the observed shift in instability models, underscores the high sensitivity of component behavior to minor differences in simulated material response. These results support that a divergence in buckling modes is the most probable outcome when the two different material models are employed, given the assumed member geometry, material properties, and imperfections in this study.

## Discussion of Results, Limitations, and Future Work

Through this paper, the proposed material model has been calibrated using multiple tests for each steel material in an effort to represent better the material's response to random strain histories, such as those expected in steel components during earthquake loading. Using this method, the proposed material model has been shown to improve the predicted stress-strain behavior over the classic Voce-Chaboche model for all the data sets considered. This comes as a result of the model's ability to reduce the yield surface while maintaining nonsoftening behavior initially. The same comparisons cannot yet be made with other structural steel material models referenced in this paper because the authors consider that meaningful comparisons can only be made when evaluating the same set of data and error measures.

Through an investigation of the component-level sensitivity to material model assumptions, this paper shows that seemingly minute differences in the material-level response can be magnified in the component-level response. This difference is mainly attributed to the difference in the initial yield stress parameter between the classic Voce-Chaboche and proposed models. The case study in this paper demonstrates that this difference in the initial yield stress may have a significant impact on simulated column instability modes. This result is notable because, to the authors' knowledge, such a result regarding CFE component-level sensitivity has not yet

been investigated for the structural steel constitutive models referenced in this paper.

The preceding considerations notwithstanding, one limitation of this work is that no rigorous assertation can presently be made on whether the modifications to the Voce-Chaboche material model result in more accurate representations of component level responses compared to test data. Although assessing the relative merits of different modeling approaches in component level experiments requires test data where the material properties are fully known (i.e., several uniaxial or multiaxial coupons have been tested with different loading protocols for both the flange and web), the geometric imperfections in the member have been measured, and the residual stresses in the section are known. To the authors' knowledge, to date, such data do not exist for any full-scale steel column test. Conducting experiments in the future that include the data noted previously is considered essential to assess and validate the material level sensitivity that has been postulated in this paper. The component-level sensitivity uncovered in this study is very likely to depend on the component under consideration; therefore, this matter should also be investigated for other steel components. Finally, the proposed model does not consider time-dependent effects (i.e., strain rate effects and strain aging). These effects, including their impact on prepeak and postpeak component behavior, should be addressed in the future.

## **Conclusions**

Prior work (de Castro e Sousa et al. 2020) shows that the calibration of the Voce-Chaboche material model parameters consistently underestimate the initial yield stress in mild steels when the calibration method is based on minimizing the difference in strain energy across multiple tests that include strain demands deemed representative of those expected in steel components subjected to earthquake loading. This issue can be attributed to the permanent decrease in the yield stress because of the discontinuous yielding phenomenon present in these metals. In this paper, we propose an UVC nonlinear isotropic/kinematic hardening material model as well as its calibration methodology. The main outcomes are summarized as follows:

- Constraints on the parameters of the UVC model are essential to ensure a hardening response consistent with the behavior of mild steels. Two constraints are formulated to ensure nonsoftening behavior regardless of the steel material.
- The material model implementation is validated in commercial and open-source finite-element analysis programs such as Abaqus (as UMATs) and OpenSees (as a UniaxialMaterial and NDMaterials) for uniaxial, plane-stress, and multiaxial stress states. The code is made publicly available (Hartloper 2019).
- Parameters for the UVC material model are provided for a database of nine structural steels used in North America, Japan, and

Europe. The initial yield stress is increased by 17% using the UVC model over the Voce-Chaboche model. A 19% relative improvement in the overall material model accuracy is found when compared to the Voce-Chaboche model. The full calibration procedure of the UVC model is made available in the open-source Python package RESSPyLab (de Castro e Sousa et al. 2019).

- At least two backstresses are necessary for the UVC model to represent the behavior of the investigated steel materials accurately. One backstress leads to an underfitting of the kinematic hardening component.
- Results from the conducted parametric study suggest that the simulated geometric instabilities in steel wide-flange columns that arise under multiaxis loading are sensitive to the material model and input parameters for the studied column geometry.
- Findings from the case study should be supported by full-scale
  tests in which the imperfections, residual stresses within the
  cross-section, and material characteristics are fully quantified
  beforehand to evaluate the effect of material initial conditions
  reliably. Furthermore, effects that influence the hardening mechanisms and spread of plasticity within the plastic hinge length of
  the columns, such as the rate of the applied loading, should also
  be explored in the future by means of large-scale physical
  testing.

# **Data Availability Statement**

Some or all data, models, or code generated or used during the study are available in a repository or online in accordance with funder data retention policies. This includes the following: the code used for the calibration procedure available in RESSPyLab (de Castro e Sousa et al. 2019), the finite-element models used for validation, and the implemented material models available in the study by Hartloper (2019).

Some or all data, models, or code that support the findings of this study are available from the corresponding author upon reasonable request. This includes the following: the finite-element models used in the case study section and the uniaxial stress-strain data used for the calibration of parameters in Tables 1 and 2.

# **Acknowledgments**

This study is based on work supported by the École Polytechnique Fédérale de Lausanne (EPFL) and by the Swiss National Science Foundation (Project No. 200021\_188476). The financial support is gratefully acknowledged. Any opinions, findings, and conclusions or recommendations expressed in this paper are those of the authors and do not necessarily reflect the view of sponsors.

#### **Notation**

The following symbols are used in this paper:

- a = isotropic hardening rate parameter for yield surface reduction;
- $a_{(\cdot)}^{(\cdot)}$  = buckling mode scale factor for geometric imperfections;
- $\vec{b}$  = isotropic hardening rate parameter for cyclic hardening;
- $\mathbf{C} = \kappa \mathbf{1} \otimes \mathbf{1} + 2\mu \mathbf{I}_{dev}$ , fourth-order tensor of elastic moduli;
- $\mathbf{C}^{ep}$  = fourth-order tensor of elastoplastic moduli;
- $C_k$  = kinematic hardening magnitude for k'th backstress;
- $D_{\infty}$  = isotropic hardening magnitude for yield surface reduction:

- $E_m$  = case study error metric;
- $e_i$  = first-order standard basis tensor;
- $e_k$  = update to kinematic hardening;
- f = von Mises yield function;
- f(x) = objective function in minimization problem;
- g(x) = vector of constraint functions;
- $g(\Delta \lambda)$  = equation for consistency condition in radial return mapping;
- $\hat{g}$ ,  $g_1$ ,  $g_2$  = constraints to ensure nonsoftening;
  - H' = kinematic hardening modulus;
    - $\mathbf{I} = 1/2(\delta_{ik}\delta_{jl} + \delta_{il}\delta_{jk})\mathbf{e}_i \otimes \mathbf{e}_j \otimes \mathbf{e}_k \otimes \mathbf{e}_l$ , fourth-order sym. identity tensor;
  - $I_{\text{dev}} = I 1/31 \otimes 1$ , fourth-order deviatoric identify tensor;
  - K' = isotropic hardening modulus;
  - M =discrete base-moment history vector;
  - $N_T$  = number of load protocols used in calibration;
    - n =unit vector-field normal to yield surface;
  - $Q_{\infty}$  = isotropic hardening magnitude for cyclic hardening;
    - T = end of time interval;
    - t = time variable;
    - x =parameter vector for proposed material model (uniaxial);
    - $\alpha$  = second-order total backstress tensor;
    - $\gamma_k$  = kinematic hardening rate parameter for k'th backstress;
  - $\Delta \lambda$  = increment in plastic multiplier;
  - $\delta_{ii}$  = Kronecker delta;
  - $\epsilon_{\text{tol}}$  = tolerance in optimization problem;
    - $\varepsilon$  = second-order strain tensor;
  - $\varepsilon^e$  = second-order elastic strain tensor;
  - $\varepsilon^p$  = second-order plastic strain tensor;
  - $\varepsilon_L$  = Luders' strain;
  - $\varepsilon_{eq}^p$  = equivalent plastic strain;
  - $\varepsilon^*$  = accumulated absolute strain;
  - $\kappa$  = bulk modulus;
  - $\lambda$  = consistency parameter (time derivative of plastic multiplier);
  - $\mu$  = shear modulus;
  - $\xi$  = second-order relative stress tensor;
  - $\rho$  = hardening metrics;
  - $\sigma$  = second-order stress tensor;
  - $\sigma_{\rm y}$  = yield stress;
  - $\sigma_{v,0}$  = initial yield stress;
    - $\bar{\varphi}$  = normalized calibration error metric;
    - $1 = \delta_{ii} e_i \otimes e_i$ , second-order identity tensor;
  - $(\cdot)$  = time derivative; and
  - $(\cdot)_{\mu/\sigma}$  = mean/standard deviation for imperfections.

#### References

ABAQUS. 2014. ABAQUS standard and ABAQUS documentation for version 6.14. Providence, RI: Dassault Systèmes Simulia.

AISC. 2016. Seismic provisions for structural steel buildings. ANSI/AISC 341-16. Chicago: AISC.

Armstrong, P. J., and C. Frederick. 1966. A mathematical representation of the multiaxial Bauschinger effect. Rep. No. RD/B/N731. London: Central Electricity Generating Board, Berkeley Nuclear Laboratories.

ASTM. 2015. Standard specification for structural steel shapes. ASTM A992/A992M-11. West Conshohocken, PA: ASTM.

ASTM. 2018. Standard terminology relating to steel, stainless steel, related alloys, and ferroalloys. ASTM A941-18. West Conshohocken, PA: ASTM.

- ATC (Applied Technology Council). 2017. Guidelines for nonlinear structural analysis and design of buildings. Part IIa: Steel moment frames. Rep. No. NIST GCR 17-917-46v2. Gaithersburg, MD: National Institute of Standards and Technology.
- ATC (Applied Technology Council). 2018. "ATC-106-1 beam column blind prediction contest." Accessed September 9, 2019. https://www.atcouncil.org/atc-106-blind-contest.
- Bierlaire, M. 2015. Optimization: Principles and algorithms. Lausanne, Switzerland: EPFL Press.
- Budaházy, V., and L. Dunai. 2013. "Parameter-refreshed Chaboche model for mild steel cyclic plasticity behaviour." *Period. Polytech. Civ. Eng.* 57 (2): 139–155. https://doi.org/10.3311/PPci.7170.
- Byrd, R. H., M. E. Hribar, and J. Nocedal. 1999. "An interior point algorithm for large-scale nonlinear programming." *SIAM J. Optim.* 9 (4): 877–900. https://doi.org/10.1137/S1052623497325107.
- CEN (European Committee for Standardization). 1993. *Structural steel I and H sections: Tolerances on shape and dimensions*. EN 10034:1993. Brussels, Belgium: CEN.
- CEN (European Committee for Standardization). 2005a. Design of steel structures part 1-1: General rules and rules for buildings. EN 1993-1-1. Brussels, Belgium: CEN.
- CEN (European Committee for Standardization). 2005b. Hot rolled products of structural steels part 2: Technical delivery conditions for nonalloy structural steels. EN 10025-2. Brussels, Belgium: CEN.
- Chaboche, J. L., K. D. Van, and G. Cordier. 1979. "Modelization of the strain memory effect on the cyclic hardening of 316 stainless steel." In *Proc.*, 5th Int. Conf. on Structural Mechanics in Reactor Technology. Amsterdam, Netherlands: North-Holland Publishing.
- Cofie, N. G., and H. Krawinkler. 1985. "Uniaxial cyclic stress-strain behavior of structural steel." *J. Eng. Mech.* 111 (9): 1105–1120. https://doi.org/10.1061/(ASCE)0733-9399(1985)111:9(1105).
- Conn, A. R., N. I. M. Gould, and P. L. Toint. 2000. Trust region methods: MOS-SIAM series on optimization. Philadelphia, PA: Society for Industrial and Applied Mathematics.
- Cottrell, A. H., and B. A. Bilby. 1949. "Dislocation theory of yielding and strain ageing of iron." *Proc. Phys. Soc. London, Sect. A* 62 (1): 49–62. https://doi.org/10.1088/0370-1298/62/1/308.
- Cravero, J., A. Elkady, and D. G. Lignos. 2020. "Experimental evaluation and numerical modeling of wide-flange steel columns subjected to constant and variable axial load couple with lateral drift demands." *J. Struct. Eng.* 146 (3): 04019222. https://doi.org/10.1061/(ASCE)ST .1943-541X.0002499.
- de Castro e Sousa, A., A. R. Hartloper, and D. G. Lignos. 2019. "RESSPy-Lab version 1.0: Python tools for structural steel research." Accessed December 21, 2020. https://pypi.org/project/RESSPyLab/.
- de Castro e Sousa, A., and D. G. Lignos. 2017. Residual stress measurements of European hot-rolled I-shaped steel profiles. Rep. No. 231302. Lausanne, Switzerland: Resilient Steel Structures Laboratory (RESSLab), EPFL.
- de Castro e Sousa, A., Y. Suzuki, and D. Lignos. 2020. "Consistency in solving the inverse problem of the Voce-Chaboche constitutive model for plastic straining." *J. Eng. Mech.* 146 (9): 04020097. https://doi.org /10.1061/(ASCE)EM.1943-7889.0001839.
- Elkady, A. 2016. "Collapse risk assessment of steel moment resisting frames designed with deep wide-flange columns in seismic regions." Ph.D. thesis, Dept. of Civil Engineering and Applied Mechanics, McGill Univ.
- Elkady, A., and D. G. Lignos. 2015. "Analytical investigation of the cyclic behavior and plastic hinge formation in deep wide-flange steel beamcolumns." *Bull. Earthquake Eng.* 13 (4): 1097–1118. https://doi.org/10 .1007/s10518-014-9640-y.
- Elkady, A., and D. G. Lignos. 2018a. "Full-scale testing of deep wide-flange steel columns under multiaxis cyclic loading: Loading sequence, boundary effects, and lateral stability bracing force demands." *J. Struct. Eng.* 144 (2): 04017189. https://doi.org/10.1061/(ASCE)ST.1943-541X.0001937.
- Elkady, A., and D. G. Lignos. 2018b. "Improved seismic design and nonlinear modeling recommendations for wide-flange steel columns." J. Struct. Eng. 144 (9): 04018162. https://doi.org/10.1061/(ASCE)ST .1943-541X.0002166.

- Fell, B. V., A. M. Kanvinde, G. G. Deierlein, and A. T. Myers. 2009. "Experimental investigation of inelastic cyclic buckling and fracture of steel braces." *J. Struct. Eng.* 135 (1): 19–32. https://doi.org/10.1061 /(ASCE)0733-9445(2009)135:1(19).
- Fogarty, J., and S. El-Tawil. 2016. "Collapse resistance of steel columns under combined axial and lateral loading." *J. Struct. Eng.* 142 (1): 04015091. https://doi.org/10.1061/(ASCE)ST.1943-541X .0001350.
- Grigoriou, V., and D. G. Lignos. 2017. Characterization of the cyclic hardening properties of European steels. Technical Rep. Lausanne, Switzerland: Resilient Steel Structures Laboratory (RESSLab), EPFL.
- Haidemenopoulos, G. N. 2018. Physical metallurgy: Principles and design. Boca Raton, FL: CRC Press.
- Hall, E. O. 1970. *Yield point phenomena in metals and alloys*. New York: Plenum Press.
- Hartloper, A. R. 2019. "UVC\_MatMod: Updated Voce-Chaboche (UVC) material model for structural steels." Accessed November 22, 2019. https://github.com/ahartloper/UVC\_MatMod.
- Hartloper, A. R., A. de Castro e Sousa, and D. G. Lignos. 2019. A nonlinear isotropic/kinematic hardening model for materials with discontinuous yielding. Rep. No. 271062. Lausanne, Switzerland: Resilient Steel Structures Laboratory (RESSLab), EPFL.
- Hartloper, A. R., and D. G. Lignos. 2019. Measurement and identification of imperfections in steel wide-flange cross-sections using point cloud data. Rep. No. 264781. Lausanne, Switzerland: Resilient Steel Structures Laboratory (RESSLab), EPFL.
- Hassan, T., and S. Kyriakides. 1992. "Ratcheting in cyclic plasticity. Part I: Uniaxial behavior." *Int. J. Plast.* 8 (1): 91–116. https://doi.org/10.1016 /0749-6419(92)90040-J.
- Hopperstad, O. S., and S. Remseth. 1995. "A return mapping algorithm for a class of cyclic plasticity models." *Int. J. Numer. Methods Eng.* 38 (4): 549–564. https://doi.org/10.1002/nme.1620380404.
- Hsiao, P.-C., D. E. Lehman, and C. W. Roeder. 2012. "Improved analytical model for special concentrically braced frames." *J. Constr. Steel Res.* 73 (Jun): 80–94. https://doi.org/10.1016/j.jcsr.2012.01.010.
- Hu, F., G. Shi, and Y. Shi. 2018. "Constitutive model for full-range elastoplastic behavior of structural steels with yield plateau: Formulation and implementation." *Eng. Struct.* 171 (Sep): 1059–1070. https://doi.org/10 .1016/j.engstruct.2016.02.037.
- Imanpour, A., R. Tremblay, A. Davaran, C. D. Stoakes, and L. A. Fahnestock. 2016. "Seismic performance assessment of multitiered steel concentrically braced frames designed in accordance with the 2010 AISC seismic provisions." *J. Struct. Eng.* 142 (12): 04016135. https://doi.org/10.1061/(ASCE)ST.1943-541X.0001561.
- Jones, E., T. Oliphant, and P. Peterson. 2001. "SciPy: Open source scientific tools for Python." Accessed November 19, 2018. http://www.scipy.org/.
- Kalochairetis, K. E., and C. J. Gantes. 2011. "Numerical and analytical investigation of collapse loads of laced built-up columns." *Comput. Struct.* 89 (11): 1166–1176. https://doi.org/10.1016/j.compstruc.2010 .10.018.
- Kanno, R. 2016. "Advances in steel materials for innovative and elegant steel structures in Japan—A review." Struct. Eng. Int. 26 (3): 242–253. https://doi.org/10.2749/101686616X14555428759361.
- Kaufmann, E. J., B. Metrovich, and A. W. Pense. 2001. Characterization of cyclic inelastic strain behavior on properties of A572 Gr. 50 and A913 Gr. 50 rolled sections. Rep. No. 01-13. Bethlehem, PA: ATLSS, Lehigh Univ.
- Lemaitre, J., and J.-L. Chaboche. 1990. *Mechanics of solid materials*. Cambridge, UK: Cambridge University Press.
- Lignos, D. G., A. R. Hartloper, A. Elkady, G. G. Deierlein, and R. O. Hamburger. 2019. "Proposed updates to the ASCE 41 nonlinear modeling parameters for wide-flange steel columns in support of performance-based seismic engineering." J. Struct. Eng. 145 (9): 04019083. https://doi.org/10.1061/(ASCE)ST.1943-541X.0002353.
- Lubliner, J. 2008. Plasticity theory. New York: Dover.
- Mahan, M., Y. F. Dafalias, M. Taiebat, Y. Heo, and S. K. Kunnath. 2011. "SANISTEEL: Simple anisotropic steel plasticity model." *J. Struct.*

- Eng. 137 (2): 185–194. https://doi.org/10.1061/(ASCE)ST.1943-541X .0000297.
- McKenna, F. T. 1997. "Object-oriented finite element programming: Frameworks for analysis, algorithms and parallel computing." Ph.D. thesis, Dept. of Civil Engineering, Univ. of California.
- Neilsen, M., and H. Schreyer. 1993. "Bifurcations in elastic-plastic materials." *Int. J. Solids Struct.* 30 (4): 521–544. https://doi.org/10.1016/0020 -7683(93)90185-A.
- Ohno, N. 1982. "A constitutive model of cyclic plasticity with a nonhardening strain region." J. Appl. Mech. 49 (4): 721–727. https://doi.org/10.1115/1.3162603.
- Schafer, B. W., Z. Li, and C. D. Moen. 2010. "Computational modeling of cold-formed steel." *Thin-Walled Struct*. 48 (10): 752–762. https://doi.org/10.1016/j.tws.2010.04.008.
- Simo, J. C., and T. J. R. Hughes. 1998. "Computational inelasticity." In *Interdisciplinary applied mathematics*. New York: Springer.
- Sowerby, R., D. Uko, and Y. Tomita. 1979. "A review of certain aspects of the Bauschinger effect in metals." *Mater. Sci. Eng.* 41 (1): 43–58. https://doi.org/10.1016/0025-5416(79)90043-0.
- Suzuki, T., Y. Yoshida, Y. Shimura, Y. Suzuki, S. Kubota, and M. Nagata. 2008. Development of building structural steel with high yield ratio

- and high yield point leading to innovative steel structural system. Rep. No. 97. Tokyo: Nippon Steel.
- Suzuki, Y. 2018. "Earthquake induced collapse of steel moment resisting frames with conventional and high performance steel columns." Ph.D. thesis, Dept. of Civil Engineering and Applied Mechanics, McGill Univ.
- Ucak, A., and P. Tsopelas. 2011. "Constitutive model for cyclic response of structural steels with yield plateau." J. Struct. Eng. 137 (2): 195–206. https://doi.org/10.1061/(ASCE)ST.1943-541X.0000287.
- Voce, E. 1948. "The relationship between stress and strain for homogeneous deformation." J. Inst. Met. 74: 537–562.
- Yoshida, F., and T. Uemori. 2002. "A model of large-strain cyclic plasticity describing the Bauschinger effect and workhardening stagnation." *Int.* J. Plast. 18 (5): 661–686. https://doi.org/10.1016/S0749-6419(01) 00050-X
- Young, B. W. 1972. "Residual stresses in hot rolled members." In Vol. 23 of International colloquium on column strength, 25–38. Paris: International Association for Bridge and Structural Engineering.
- Ziemian, R. D., J. C. Batista Abreu, M. D. Denavit, and T.-J. L. Denavit. 2018. "Three-dimensional benchmark problems for design by advanced analysis: Impact of twist." *J. Struct. Eng.* 14 (12): 04018220. https://doi.org/10.1061/(ASCE)ST.1943-541X.0002224.